A&A 638, A136 (2020)
https://doi.org/10.1051/0004-6361/202037742

Astronomy & Astrophysics

X-raying winds in distant quasars: The first high-redshift wind duty cycle

E. Bertola[1,2], M. Dadina[2], M. Cappi[2], C. Vignali[1,2], G. Chartas[3], B. De Marco[4], G. Lanzuisi[2], M. Giustini[5], and E. Torresi[2]

[1] Dipartimento di Fisica e Astronomia, Università degli Studi di Bologna, Via P. Gobetti 93/2, Bologna 40129, Italy
e-mail: elena.bertola2@unibo.it
[2] INAF–OAS, Osservatorio di Astrofisica e Scienza dello Spazio di Bologna, Via P. Gobetti 93/3, Bologna 40129, Italy
[3] Department of Physics and Astronomy of the College of Charleston, Charleston, SC 29424, USA
[4] N. Copernicus Astronomical Center of the Polish Academy of Sciences, Bartycka 18, Warsaw 00-716, Poland
[5] Centro de Astrobiología (CSIC-INTA), Camino Bajo del Castillo s/n, Villanueva de la Cañada, Madrid 28692, Spain

Received 14 February 2020 / Accepted 24 April 2020

ABSTRACT

Aims. Theoretical models of wind-driven feedback from active galactic nuclei (AGN) often identify ultra-fast outflows as being the main agent in the generation of galaxy-sized outflows, which are possibly the main actors in establishing so-called AGN-galaxy co-evolution. Ultra-fast outflows are well characterized in local AGN but much less is known in quasars at the cosmic time when star formation and AGN activity peaked ($z \simeq 1$–3). It is therefore necessary to search for evidence of ultra-fast outflows in high-z sources to test wind-driven AGN feedback models.
Methods. Here we present a study of Q2237+030, the Einstein Cross, a quadruply-imaged radio-quiet lensed quasar located at $z = 1.695$. We performed a systematic and comprehensive temporally and spatially resolved X-ray spectral analysis of all the available *Chandra* and *XMM-Newton* data (as of September 2019).
Results. We find clear evidence for spectral variability, possibly due to absorption column density (or covering fraction) variability intrinsic to the source. For the first time in this quasar, we detect a fast X-ray wind outflowing at $v_{\rm out} \simeq 0.1c$ that would be powerful enough ($\dot{E}_{\rm kin} \simeq 0.1\,L_{\rm bol}$) to significantly affect the evolution of the host galaxy. We report also on the possible presence of an even faster component of the wind ($v_{\rm out} \sim 0.5c$). For the first time in a high-z quasar, given the large sample and long time interval spanned by the analyzed X-ray data, we are able to roughly estimate the wind duty cycle as $\simeq$0.46 (0.31) at 90% (95%) confidence level. Finally, we also confirm the presence of a Fe Kα emission line with variable energy, which we discuss in the light of microlensing effects as well as considering our findings on the source.

Key words. galaxies: high-redshift – quasars: individual: Q2237+030 – quasars: absorption lines – X-rays: general

1. Introduction

Since the discovery of the existence of scaling relations between the mass of super massive black holes (SMBH) and the global properties of their host galaxy bulge (e.g., the $M_{\rm BH} - \sigma$ relation; McConnell et al. 2011, and references therein), feedback from the active galactic nucleus (AGN) is often invoked as a key ingredient in regulating both the star formation (SF) activity in the host galaxy and the growth of the SMBH itself. Despite its importance, we still lack a full understanding of AGN feedback (Kormendy & Ho 2013).

Current models (e.g., King & Pounds 2015) predict that the co-evolution of SMBHs and their host galaxy might be initiated by the generation of fast accretion-disk winds, which could evolve into massive galaxy-scale outflows, possibly quenching the host galaxy star formation by sweeping out all of its interstellar medium (ISM). To provide efficient AGN feedback, the inner winds need to be accelerated at sufficient speed (nominally at semi-relativistic velocities) and need to carry a mechanical power higher than the minimum threshold set by the models at an approximate value of 0.5%–5% $L_{\rm bol}$ (e.g., Di Matteo et al. 2005; Hopkins & Elvis 2010). In the past decade, these inner winds have often been observationally identified with ultra-fast outflows (UFOs; Tombesi et al. 2010, 2011, 2012, 2013; Gofford et al. 2013), which are the most extreme winds known to date, characterized by the highest outflow velocities (up to 0.2–0.3c). They have been discovered in the X-ray band, through their characteristic blueshifted iron resonant absorption lines above $\simeq$7 keV, and they are thought to arise at sub-parsec scales then expand in the surrounding ISM.

Besides probing how the inner-disk winds can trigger galaxy-scale outflows (Fiore et al. 2017; Smith et al. 2019; Mizumoto et al. 2019), we are also still struggling to constrain the occurrence rate of UFOs. They have been mostly studied in bright and nearby Seyfert galaxies, leading to a detection fraction of $\simeq$40–50% (Tombesi et al. 2010, but see also Igo et al. 2020). Moreover, clear variability from one observation to the other (Cappi et al. 2009) and also within single observations (Giustini et al. 2011; Gofford et al. 2014) has been observed, with variations happening on timescales as short as a few kiloseconds. Thus, the current idea is that UFOs might well be common and widespread, but episodic events. However, we are still lacking robust statistical studies of their average properties in the distant Universe. In particular, it is of extreme relevance to fill the gap at those redshifts where the SMBH and bulge scaling relations are thought to be shaped,

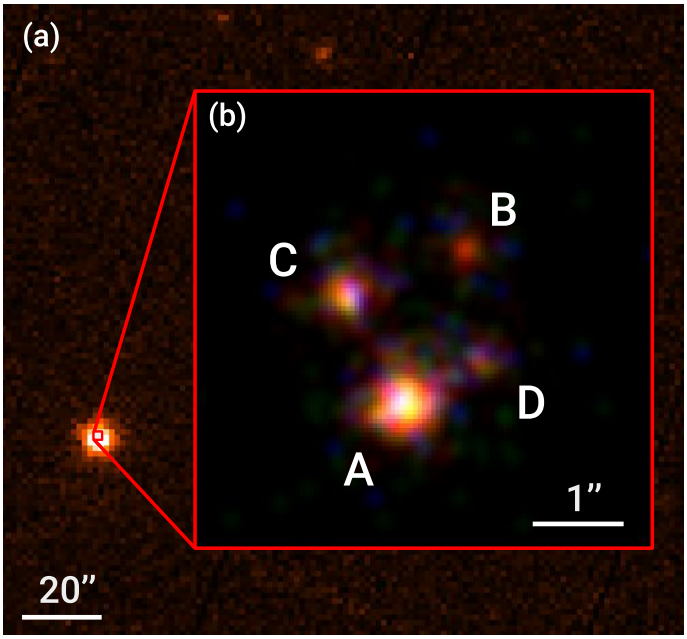

Fig. 1. (a) EPIC-pn cleaned image of XMM 2002 in the 0.3–10 keV observed-energy band. The red square marks the 5″ region of the *Chandra* image centered on the quasar and shown in inset (b). (b) Raw *Chandra* image of Q2237+030 (ObsID 431) binned with a bin size of 0.1″, color-coded based on the observed-energy bands: 0.4–2 keV in red, 2–4.5 keV in green, and 4.5–7 keV in blue. The images are named A, B, C, and D as in Yee (1988). Given the quasar redshift ($z_Q = 1.695$), 1″ separation corresponds to a distance of 8.68 kpc (cosmology values: $H_0 = 70.0\,\mathrm{km\,s^{-1}\,Mpc^{-1}}$, $\Lambda_0 = 0.73$).

that is, where we expect the feedback processes to be most relevant and possibly visible. This corresponds to the cosmic time at which starburst and AGN activity peaked, the so-called cosmic noon ($z \simeq 1$–3). So far, only very few sources at $z \geq 1.5$ have been analyzed with this goal in the X-ray band, namely APM 08279+5255, PG1115+080, H1413+117, HS 0810+2554, and MG J0414+0534 (Hasinger et al. 2002; Chartas et al. 2003, 2007, 2016a; Dadina et al. 2018). Interestingly, almost all UFO detections at $z > 0.1$ are associated with gravitationally lensed quasars (GLQs), and, to our knowledge, thus far the only bright, unlensed sources at $z \geq 1.5$ are PID352 and HS 1700+6416 (Vignali et al. 2015; Lanzuisi et al. 2012). That high-redshift UFOs are associated with GLQs is not surprising given that good signal-to-noise spectra are needed to determine the presence of these winds. In this sense, the magnification provided by the gravitational lens is a unique tool to obtain good quality data in a sustainable amount of observational time.

In this work, we performed a new and extensive study of a high-z GLQ: the Einstein Cross (Q2237+030, hereafter Q2237), a quadruply imaged quasar at $z_q = 1.695$ (lens at $z_l = 0.039$). Discovered by Huchra in 1985 (Huchra et al. 1985), Q2237 was detected for the first time in the X-ray band in 1997 by the high resolution camera on board of ROSAT (Wambsganss et al. 1999) but *Chandra* was the first X-ray facility capable of resolving the four images of the quasar (Dai et al. 2003). Being the first GLQ with a nearby lens to have ever been discovered, it was soon recognized as a unique case to study both macro- and microlensing properties. It has thus been the target of many microlensing monitoring campaigns, first in the optical, then, after the advent of *Chandra*, also in the X-ray, enabling an investigation of the size of the quasar's emitting regions in both bands (e.g., Mosquera et al. 2013; Guerras et al. 2017). Gravitational lensing theoretical models for this system agree on predicting time delays between the four source images (A, B, C, D, as named in Yee 1988, see Fig. 1) of shorter than a day ($\Delta t_{AB} \approx 2$ h, $\Delta t_{AC} \approx -16$ h, $\Delta t_{AD} \approx -5$ h) and a global magnification factor[1] of $\mu \approx 16$ (Schmidt et al. 1998; Wertz & Surdej 2014). Dai et al. (2003) succeeded in confirming the shortest time delay ($\Delta t_{AB} = 2.7^{+0.5}_{-0.9}$ h) through the *Chandra* data. Q2237 has also been studied in the X-ray band to assess its spectral properties, either over single observations, from *Chandra* (Chen et al. 2012) and *XMM-Newton* (Fedorova et al. 2008), or from *Chandra* spectra stacked over multiple observations, both keeping the images separate (Dai et al. 2003; Chen et al. 2012) and summing all the images (Chen et al. 2012; Reynolds et al. 2014). In this work, we carry out the first systematic and comprehensive temporally and spatially resolved X-ray spectral analysis of this source, taking advantage of the rather complementary strengths that characterize the two X-ray facilities. In Sect. 2 we list the analyzed data and present the reduction procedures. The *Chandra* and the *XMM-Newton* spectra are first analyzed separately in Sects. 3 and 4, respectively, then all the results are combined and discussed in Sect. 5. Additional results obtained from the *Chandra* stacked spectra are presented in Appendix A. Throughout the paper, we assume a flat ΛCDM cosmology (Planck Collaboration VI 2020), with $H_0 = 70.0\,\mathrm{km\,s^{-1}\,Mpc^{-1}}$ and $\Lambda_0 = 0.73$.

2. Data reduction

We collected, reduced, and analyzed all available X-ray data of Q2237 as of September 2019: 40 archival observations in total, 37 from *Chandra* and 3 from *XMM-Newton* (hereafter, XMM 2002, XMM 2016, and XMM 2018), spanning over 18 years (≃6.7 yr in the quasar rest frame), for a total of ≃0.9 Ms exposure. The Einstein Cross was the target of each pointing, so it is always observed on-axis. Tables 1 and 2 summarize the main information of all the observations. The *Chandra* observations show exposure times ranging from 7.3 ks to 34.2 ks, while those of *XMM-Newton* are much longer (42.9 ks, 24.9 ks, and 141.6 ks, in chronological order). None of the observations provide simultaneous *Chandra* and *XMM-Newton* data; the time elapsed between each *XMM-Newton* pointing and the closest *Chandra* observation ranges from one to six months. Since one of the main goals of the present work is to search for and robustly assess (through appropriate statistical tests and simulations) the presence of feedback and the significance of wind-related features in the X-ray spectra of the Einstein Cross, the lack of simultaneity between the *Chandra* and *XMM-Newton* data does not influence the results of this work. Conversely, this lack turns out to be quite convenient in assessing the recurrence of these features at different epochs and will allow us to investigate their presence on a more extended time baseline.

The use of data from both facilities is fundamental to our goal for the following reasons. On the one hand, given the superb angular resolution of *Chandra*, with its data we can carry out a spectral analysis that is spatially resolved over the single images of the quasar (see Fig. 1). On the other hand, *XMM-Newton* provides high counting-statistics spectra, by means of its larger effective area, which allows us to investigate the spatially integrated source emission through more complex and physical spectral models. All the data were reduced through the

[1] Macro-magnification of the individual images: $\mu_A \simeq 4.6$, $\mu_B \simeq 4.5$, $\mu_C \simeq 3.8$, and $\mu_D \simeq 3.6$ (Schneider et al. 1988).

Table 1. Information of each *Chandra* observation and details of the individual-image spectra.

ObsID	Date	Exposure	A_{cts}	B_{cts}	C_{cts}	D_{cts}	A_{CR}	B_{CR}	C_{CR}	D_{CR}
431	2000-09-06	30.29	⋆1272 ± 36	233 ± 15	⋆523 ± 23	177 ± 13	41.99 ± 1.18	7.69 ± 0.50	17.26 ± 0.26	5.84 ± 0.44
1632	2001-12-12	9.54	309 ± 18	51 ± 7	99 ± 10	52 ± 7	32.39 ± 1.84	5.34 ± 0.75	10.38 ± 1.04	5.45 ± 0.76
6831	2006-01-09	7.27	97 ± 10	86 ± 9	26 ± 5	35 ± 6	13.35 ± 1.36	11.83 ± 1.28	3.57 ± 0.70	4.82 ± 0.81
6832	2006-05-01	7.94	211 ± 15	111 ± 11	90 ± 10	58 ± 8	26.58 ± 1.83	13.98 ± 1.33	11.34 ± 1.19	7.31 ± 0.96
6833	2006-05-27	7.95	118 ± 11	56 ± 7	54 ± 7	21 ± 5	14.83 ± 1.37	7.04 ± 0.94	6.79 ± 0.92	2.64 ± 0.58
6834	2006-06-25	7.94	272 ± 16	111 ± 11	74 ± 9	54 ± 7	34.26 ± 2.07	13.98 ± 1.33	9.32 ± 1.08	6.80 ± 0.93
6835	2006-07-21	7.87	319 ± 18	79 ± 9	64 ± 8	49 ± 7	40.52 ± 2.27	10.03 ± 1.13	8.13 ± 1.02	6.22 ± 0.89
6836	2006-08-17	7.93	170 ± 13	62 ± 8	60 ± 8	40 ± 6	21.43 ± 1.64	7.82 ± 0.99	7.56 ± 0.98	5.04 ± 0.80
6837	2006-09-16	7.95	166 ± 13	62 ± 8	39 ± 6	35 ± 6	20.89 ± 1.62	7.80 ± 0.99	4.91 ± 0.79	4.40 ± 0.74
6838	2006-10-09	7.99	157 ± 13	53 ± 7	51 ± 7	34 ± 6	19.65 ± 1.57	6.63 ± 0.91	6.38 ± 0.89	4.26 ± 0.73
6839	2006-11-29	7.87	⋆538 ± 23	189 ± 14	108 ± 10	113 ± 11	68.32 ± 2.95	24.00 ± 1.75	13.71 ± 1.32	14.35 ± 1.35
6840	2007-01-14	7.98	441 ± 21	132 ± 11	118 ± 11	84 ± 9	55.29 ± 2.63	16.55 ± 1.44	14.79 ± 1.36	10.53 ± 1.15
11534	2009-12-31	28.46	⋆1756 ± 42	454 ± 21	164 ± 13	⋆802 ± 28	61.70 ± 1.47	15.95 ± 0.75	5.76 ± 0.45	28.18 ± 1.00
11535	2010-04-25	29.43	377 ± 19	101 ± 10	52 ± 7	150 ± 12	12.81 ± 0.66	3.43 ± 0.34	1.76 ± 0.25	5.10 ± 0.42
11536	2010-06-27	27.89	342 ± 19	105 ± 10	44 ± 7	163 ± 13	12.26 ± 0.66	3.76 ± 0.37	1.57 ± 0.24	5.84 ± 0.46
11537	2010-08-07	29.36	228 ± 15	68 ± 8	44 ± 7	116 ± 11	7.76 ± 0.51	2.31 ± 0.28	1.50 ± 0.23	3.95 ± 0.37
11538	2010-10-02	29.36	⋆501 ± 22	154 ± 12	49 ± 7	423 ± 21	17.06 ± 0.76	5.22 ± 0.42	1.67 ± 0.24	14.41 ± 0.70
11539	2010-11-23	9.83	93 ± 10	31 ± 6	13 ± 4	40 ± 6	9.46 ± 0.98	3.15 ± 0.57	1.32 ± 0.37	4.09 ± 0.64
13195	2010-11-26	9.83	91 ± 10	23 ± 5	10 ± 3	27 ± 5	9.25 ± 0.97	2.34 ± 0.49	1.01 ± 0.32	2.74 ± 0.53
13191	2010-11-27	9.83	82 ± 9	19 ± 4	9 ± 3	29 ± 5	8.34 ± 0.92	1.93 ± 0.44	0.91 ± 0.31	2.95 ± 0.55
12831	2011-05-14	29.36	⋆2677 ± 52	⋆575 ± 24	215 ± 15	429 ± 21	91.19 ± 1.76	19.58 ± 0.82	7.32 ± 0.50	14.61 ± 0.71
12382	2011-12-27	29.79	343 ± 19	128 ± 11	59 ± 8	100 ± 10	11.51 ± 0.62	4.29 ± 0.38	1.98 ± 0.26	3.36 ± 0.34
13960	2012-01-09	29.36	308 ± 18	122 ± 11	52 ± 7	117 ± 11	10.49 ± 0.60	4.15 ± 0.38	1.77 ± 0.25	3.98 ± 0.37
13961	2012-08-02	29.24	⋆906 ± 30	244 ± 16	213 ± 15	202 ± 14	30.98 ± 0.10	8.34 ± 0.53	7.28 ± 0.50	6.91 ± 0.49
14513	2012-12-26	28.62	⋆684 ± 26	247 ± 16	339 ± 18	260 ± 16	23.89 ± 0.91	8.26 ± 0.55	11.84 ± 0.64	9.08 ± 0.56
14514	2013-01-05	29.36	⋆622 ± 26	215 ± 15	298 ± 17	268 ± 16	21.18 ± 0.85	7.32 ± 0.50	10.15 ± 0.59	9.13 ± 0.56
14515	2013-08-31	9.73	164 ± 22	57 ± 8	62 ± 8	30 ± 5	16.85 ± 1.32	5.86 ± 0.78	6.37 ± 0.81	3.08 ± 0.56
16316	2013-08-26	9.83	120 ± 11	44 ± 7	47 ± 7	30 ± 5	12.21 ± 1.11	4.48 ± 0.68	4.78 ± 0.70	3.05 ± 0.56
16317	2013-08-28	9.83	105 ± 10	43 ± 7	45 ± 7	24 ± 5	10.68 ± 1.04	4.37 ± 0.67	4.58 ± 0.68	2.44 ± 0.50
14516	2013-10-01	29.35	230 ± 15	122 ± 11	70 ± 8	96 ± 10	7.83 ± 0.52	4.15 ± 0.38	2.38 ± 0.29	3.27 ± 0.33
14517	2014-05-14	29.36	⋆1071 ± 33	384 ± 20	322 ± 18	156 ± 12	36.48 ± 1.11	13.08 ± 0.67	10.97 ± 0.61	5.31 ± 0.43
14518	2014-06-08	29.28	⋆628 ± 25	263 ± 16	206 ± 14	117 ± 11	21.45 ± 0.86	8.98 ± 0.55	7.03 ± 0.49	3.99 ± 0.37
18804	2016-04-24	28.60	⋆1009 ± 32	269 ± 16	132 ± 11	126 ± 11	35.28 ± 1.11	9.40 ± 0.57	4.61 ± 0.40	4.41 ± 0.39
19638	2016-12-22	33.34	302 ± 17	120 ± 11	51 ± 7	77 ± 9	9.05 ± 0.52	3.60 ± 0.33	1.53 ± 0.21	2.31 ± 0.26
19639	2017-01-04	32.92	249 ± 16	113 ± 11	46 ± 7	68 ± 8	7.56 ± 0.48	3.43 ± 0.32	1.40 ± 0.21	2.06 ± 0.25
19640	2017-12-20	34.23	402 ± 20	210 ± 14	76 ± 9	94 ± 10	11.74 ± 0.59	6.13 ± 0.42	2.22 ± 0.26	2.74 ± 0.28
19641	2018-01-14	34.23	368 ± 19	170 ± 13	92 ± 10	77 ± 9	10.75 ± 0.56	4.96 ± 0.38	2.10 ± 0.25	2.25 ± 0.26

Notes. The spectra with more than 500 counts are marked with a star (high-statistics sample – HSS). The observations are listed from earliest to latest date. The exposure time is given in units of kiloseconds. The image net (i.e., background-subtracted) counts and CRs are referred to the 0.4–7 keV observed-energy range. The count rates are given in units of 10^{-3} cts s^{-1}.

Table 2. Information of each *XMM-Newton* observation of Q2237+030.

...	ObsID	Date	Exposure	Cleaned exposure	Net counts	Net CR
XMM 2002	0110960101	2002-05-28	42.87	23.53	3837 ± 62	16.3 ± 0.3
XMM 2016	0781210201	2016-11-26	24.90	6.58	683 ± 26	10.4 ± 0.4
XMM 2018	0823730101	2018-05-19	141.60	108.00	6569 ± 81	6.0 ± 0.1

Notes. The exposure time and the cleaned exposure are given in units of kiloseconds. The source net (i.e., background-subtracted) counts and CRs are referred to the EPIC-pn spectra in the 0.3–10 keV observed-energy band. The net CR is given in units of 10^{-2} cts s^{-1}.

respective standard pipelines, using CIAO 4.9 and SAS 16.1, so as to uniformly apply the latest calibrations to all observations. To extract individual image spectra from the *Chandra* data, we selected the four circular regions ($r_{A,B,C} = 0.8''$ and $r_D = 0.6''$, with encircled energy fraction – EEF – at 1.5 keV of 90% and 80%, respectively) imposing a certain offset with regard to the image centroids so as to limit the contamination from neighboring images. The background extraction region was selected as a source-free circle of 50″ radius in the same chip as the target. Furthermore, to consistently analyze the data, we adopted the same regions for all the *Chandra* observations, after checking that they actually corresponded to the emission peak of the individual components in each pointing.

Regarding the *XMM-Newton* data, we used as extraction regions a 25″ radius circle for the source ($EEF_{Epn} \simeq 85\%$ at 1.5 keV) and an 80″ radius circle for the background in all the *XMM-Newton* observations. While the background in *Chandra* is extremely low (below 0.2% of the total counts), the

first two *XMM-Newton* observations were significantly affected by soft-p$^+$ flares. Operationally, we filtered the data against different count rate thresholds (CRT), then we extracted the source and background EPIC-pn spectra for each CRT and inspected how the latter relate to the former. The best good-time-interval filtering threshold of the EPIC-pn data was then selected as that yielding a deviation of at least a factor of two between the background-subtracted source spectrum and the background spectrum in the 2–8 keV observed-energy range (~5.4–22 keV rest frame). We managed to match our criteria and obtain good quality data for XMM 2002 EPIC-pn (CRT = 5.0 cts s^{-1}, $S_{\rm cts}$ = 918 ± 30 cts in the 2–8 keV observed-energy band). Regarding XMM 2016 EPIC-pn, mainly due to the combination of high flares and the shorter exposure of this observation, the good-time-interval filtering threshold that satisfies our condition (CRT = 2.0 cts s^{-1}, $S_{\rm cts}$ = 200 ± 14 cts in the 2–8 keV observed-energy band) drastically reduces the source net counts in the energy band of interest. Since *XMM-Newton* data is the integration over the four images of the quasar, we left this observation out of our analysis since the counting statistics of the yielded source spectrum undoes the advantages provided by using *XMM-Newton* data. Regarding the EPIC-MOS data, we applied the same procedure as for the EPIC-pn, using the same extraction regions (EEF$_{\rm EMOS}$ ≃ 80% at 1.5 keV). We obtained good quality data for both cameras in XMM 2002 (CRT = 1.0 cts s^{-1}, $S_{\rm cts}$ = 440 ± 21 cts and $S_{\rm cts}$ = 412 ± 20 cts, for MOS1 and MOS2 respectively, in the 2–8 keV observed-energy band). For completeness, we applied this procedure also on XMM 2016 EPIC-MOS 1 and 2 but, as expected given the results for the EPIC-pn spectrum and the lower effective area that EPIC-MOS 1 and 2 provide, we only managed to confirm the exclusion of this observation due to the low counting statistic spectra obtained. XMM 2018, instead, shows a more stable background that allowed us to select the good-time-interval threshold directly from the detector light curves (CRT = 0.9 cts s^{-1} and CRT = 0.2 cts s^{-1} for EPIC-pn and EPIC-MOS, respectively). The properties of the cleaned *XMM-Newton* data are listed in Table 2.

2.1. Single-image multi-epoch Chandra light curves

We produced the *Chandra* single-image multi-epoch light curves by computing the image mean count rate (CR), shown in Fig. 2, versus the respective observation date. Each image presents flux variations up to a factor of ≃4 between observations. At first glance, the mean count rates seem to vary with similar trends for all the four images. However, when taking a closer look, discrepancies between the four light curves can be seen. In fact, as expected due to the proximity of the lensing galaxy ($z_{\rm l}$ = 0.039) and as found by Chen et al. (2011, 2012) and Dai et al. (2003) through flux-ratio analysis, Q2237 presents microlensing events in the X-ray band that are expected to last a few months (Mosquera & Kochanek 2011). Moreover, Dai et al. (2003) also found that more than one image of the Einstein Cross can undergo a microlensing event during a single observation. The intrinsic variability timescale of the quasar, having a ≃$1.2 \times 10^9\,M_\odot$ black hole (BH) mass (Assef et al. 2011), is much longer than all the image time delays induced by the lens (Dai et al. 2003; Schmidt et al. 1998).

Therefore, the dissimilarities between the light curves in Fig. 2 at a given epoch are likely due to microlensing (Chen et al. 2011). The effect of a microlensing event is to selectively magnify the emission arising from that particular portion of the background source that is behind the caustic. This results in a perturbation of the macrolensing-magnified image flux and is most relevant for the images with lower macro-magnification. An outflowing absorber moving along our line of sight (LOS) may produce detectable blueshifted absorption lines of highly ionized iron. We then expect microlensing events, when present, to result in a dilution of these absorption lines since they would magnify the unabsorbed emission regions that do not lie along our LOS. Microlensing events can then be considered as a competing effect to the detection of the UFO signatures in which we are mainly interested. In this regard, microlensing events are unlikely to produce fake UFO absorption lines in our spectra or to shift their energy. Although a thorough analysis of the microlensing events is beyond the scope of our work, their effect on highly blueshifted absorption lines would be an interesting numerical simulation topic for a future project.

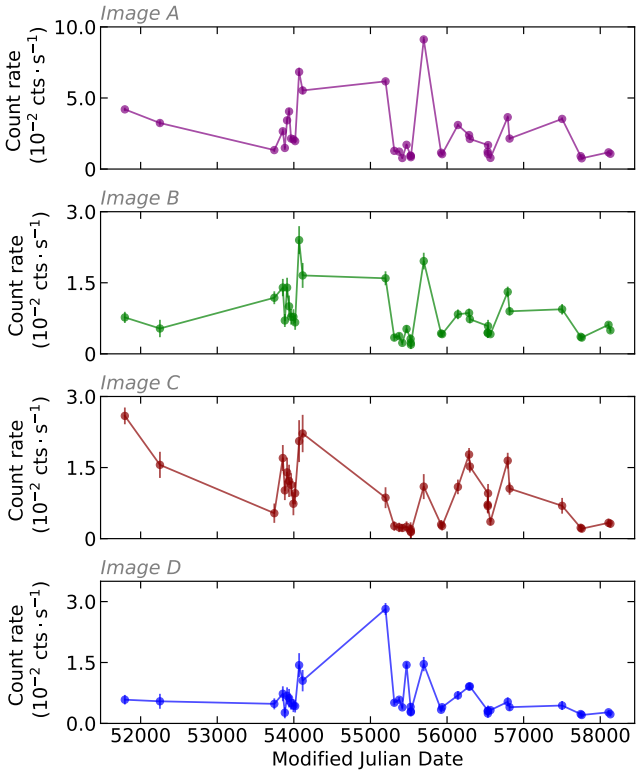

Fig. 2. *Chandra* individual-image multi-epoch light curves. We show the mean count rate between 0.4 and 7.0 keV observed frame of each observation vs. time. *From top to bottom*: image A, image B, image C, image D. The error bars are derived from the error on the Poisson-distributed counts.

2.2. XMM-Newton light curves

Since the BH mass of Q2237 is estimated to be on the order of $10^9\,M_\odot$ (Assef et al. 2011), we do not expect much short timescale variability (<1%, Ponti et al. 2012). As a sanity check, we produced the background-subtracted source light curves for the two longest observations available, XMM 2002 and XMM 2018. We grouped the light curves into 200s time bins, and split them into soft-energy (0.3–2 keV) and hard-energy (2–10 keV) bands, excluding all the background-dominated time bins (those at the beginning and at the end of the observation). The soft-band light curves are variable at the 95% confidence level both for XMM 2002 and XMM 2018. The hard-band light curves are more stable, being variable at the 28% confidence

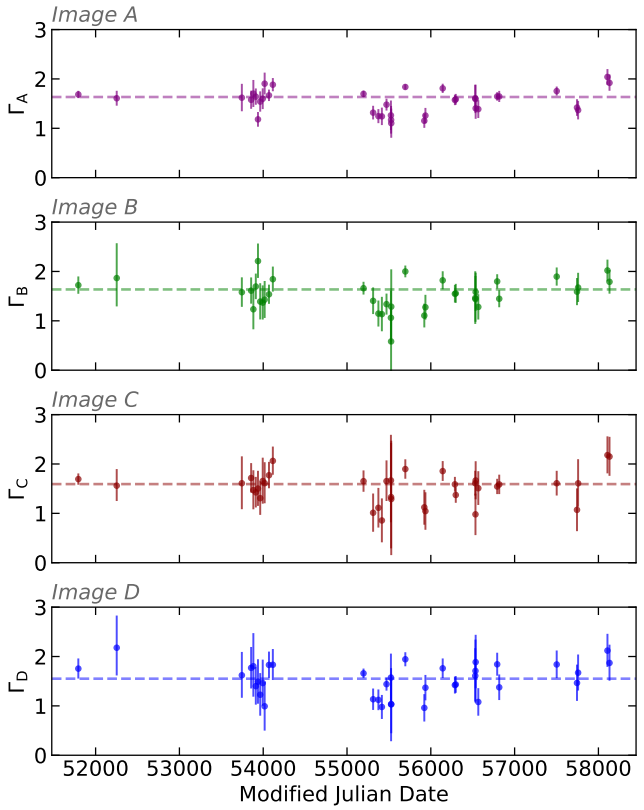

Fig. 3. Variation of the photon index (1σ errors) for each image in the *Chandra* data as a function of time. The dashed line represents the best fit obtained using a constant function.

level in XMM 2002 and at 34% in XMM 2018. Therefore we did not deem it necessary to split the observations based on the source variability, so we extracted the time-averaged spectra integrated over all the observations.

3. *Chandra* spectral analysis

We first fitted each spectrum with a single power-law model (Model `pl=phabs*zpo`), modified by Galactic absorption ($N_{\rm H} = 5.1 \times 10^{20}$ cm^{-2}; Kalberla et al. 2005), restricting the spectral fitting to the 0.4–7 keV observed-energy range (1–19 keV rest-frame energy range). The analysis of the *Chandra* spectra was then narrowed down to those with the highest counting statistics to better constrain the presence of absorption or narrow emission and absorption features. For what concerns the lower signal-to-noise ratio (S/N) data, we analyzed their stacked spectra including all the *Chandra* observations, as reported in Appendix A.

3.1. X-ray continuum spectral variability

The *Chandra* data allowed us to probe the source spectral variability on timescales of weeks to years. Figure 3 shows the best-fit photon index Γ_i (i= A, B, C, D) obtained with Model `pl` as a function of time. The maximum photon-index variation, in terms of difference between the highest and the lowest Γ_i values, changes from image to image, with image A showing the smallest ($\Delta\Gamma_{\rm A} \approx 0.94$) and image B the largest ($\Delta\Gamma_{\rm B} \approx 1.63$) variations. By fitting with a constant (dashed lines in Fig. 3), the spectral slope was found to be significantly variable (>99.9% confidence) in each image. Considering the ratios of the Γ_i, we can check whether the photon-index variations are intrinsic (if common to all images) or induced by microlensing. We find the ratios consistent with being constant overall and approximately equal to one. This agrees with the approximation applied by Chen et al. (2012), who analyzed the first 20 *Chandra* observations of our list linking the photon index of the four images at any given epoch. Moreover, the maximum Γ variations of all the images are consistent with each other when propagating their 1σ errors, thus no image shows a significantly higher maximum photon-index variation with regard to the others. Therefore, we can assume the variations of the continuum to be overall consistent between the four images, meaning they are not induced by microlensing but are inherent to the quasar.

To investigate the presence of any intrinsic spectral variability, we restricted our analysis to the high-statistics sample (HSS) to better constrain the best-fit spectral parameters. This sub-sample is made up of the fourteen spectra that show more than 500 source net counts in the 0.4–7 keV observed-energy range (those marked by a star in Table 1). The count threshold was selected to allow us to apply χ^2 statistics after binning the source spectra to at least 20 cts/bin. Fourteen spectra were extracted from eleven observations, since in three epochs (ObsIDs 431, 11534, 12831) two images exceed our threshold. In Fig. 4 we show three representative HSS spectra: that with the most counts (ObsID 12831 A), one of those with the least (ObsID 431 C), and one with an intermediate number of counts (ObsID 14517). Spectra with lower counting statistics were used to produce stacked spectra, both keeping the images separate and combining the four images, the results of which are presented in Appendices A.1 and A.2, respectively. We anticipate that the results obtained with the stacked spectra are overall consistent with the ones presented here.

To search for additional spectral continuum complexities for the HSS, we first modified Model `pl` by adding a `zphabs` component, accounting for photo-electric absorption of the primary emission in a cold medium (Model `pl_a=phabs*zphabs*zpo`), which we placed at the quasar's redshift. We find that only four spectra[2] of the HSS require extra absorption at more than a 99% confidence level (evaluated through the F-test), while for the other ten we could only derive an upper limit to such additional column density. All the best-fit values and the respective F-test significance are listed in Table 3, with those at more than a 99% confidence level shown in boldface. Among the four spectra that significantly require some extra absorption, two are referred to two images from the same epoch (ObsID 11534 image A and D) and show consistent column densities within 1σ errors. Considering only the cases where extra absorption is required by the data, we find the column density to be variable at more than a 99% confidence throughout the three epochs. To test the assumption regarding the location of the absorber, we compared the results obtained for the two spectra (ObsID 11534 A and 11538 A) showing the largest variation in column-density values by plotting their 90% confidence contours of $N_{\rm H}$ as a function of the photon index. As shown in Fig. 5, their column densities are not consistent, while their photon indices are. Furthermore, the time interval between the two observations (see Table 1) is ~275 d in the observed frame, which means ~102 d $\simeq$ 0.3 yr in the quasar rest frame. Considering that the two spectra refer to the same image, we interpret the $N_{\rm H}$ discrepancy and the short time elapsed as indications of the extra absorption being dominated by the component at the redshift of the quasar.

[2] ObsIDs 11534 A and D, 11538 A, 18804 A.

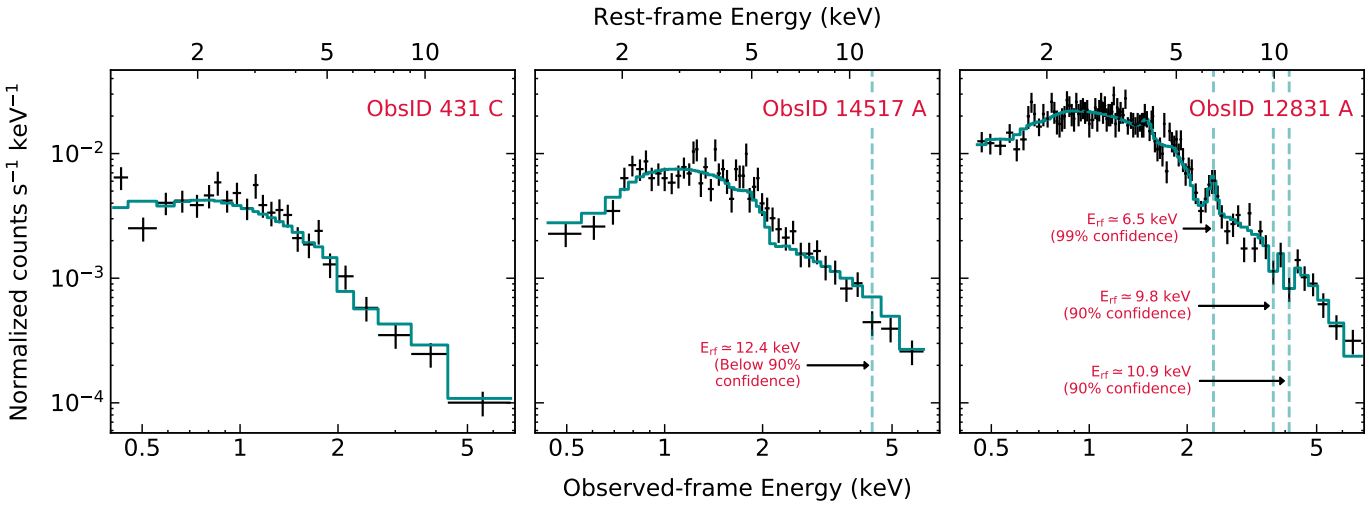

Fig. 4. Data (black) and best-fit model (blue) for three of the *Chandra* HSS spectra, representative of three statistics regimes. *From left to right*: ObsID 431 C (least counts), 14517 A (intermediate counts), and 12831 A (highest counts). The dashed vertical lines indicate the energies of the emission and absorption lines found by adopting the blind-search method of Tombesi et al. (2010). Only those above 90% confidence were included in the best-fit models (i.e., those in Tables 4a and 4b).

Table 3. Summary of the best-fit parameters for Model pl_a (`phabs*zphabs*zpowerlw`) when applied to the high-statistics sample.

ObsID	Γ	$N_{\rm H}$	$\Delta\chi^2$	Confidence
431 A	$1.86^{+0.12}_{-0.12}$	$0.34^{+0.20}_{-0.20}$	8.4	98.8%
431 C	$1.90^{+0.42}_{-0.36}$	$0.53^{+0.23}_{-0.20}$	5.9	97.7%
6839 A	$1.80^{+0.20}_{-0.20}$	$0.46^{+0.52}_{-0.42}$	3.2	84.6%
11534 A	$1.91^{+0.11}_{-0.10}$	$0.62^{+0.29}_{-0.25}$	19.3	**>99.99%**
11534 D	$2.01^{+0.20}_{-0.18}$	$1.28^{+0.57}_{-0.48}$	24.3	**>99.99%**
11538 A	$2.06^{+0.28}_{-0.26}$	$2.88^{+1.40}_{-1.17}$	22.0	**99.9%**
12831 A	$1.98^{+0.09}_{-0.09}$	$0.27^{+0.22}_{-0.21}$	4.7	96.7%
12831 B	$2.10^{+0.27}_{-0.24}$	$0.50^{+0.60}_{-0.49}$	2.9	95.6%
13961 A	$2.02^{+0.18}_{-0.16}$	$0.67^{+0.53}_{-0.44}$	7.0	97.7%
14513 A	$1.80^{+0.20}_{-0.18}$	$0.88^{+0.67}_{-0.56}$	7.1	98.4%
14514 A	$1.79^{+0.22}_{-0.20}$	$0.77^{+0.80}_{-0.66}$	3.7	85.6%
14517 A	$1.79^{+0.14}_{-0.13}$	$0.59^{+0.49}_{-0.40}$	6.5	97.2%
14518 A	$1.84^{+0.24}_{-0.22}$	$1.01^{+1.03}_{-0.84}$	4.1	96.5%
18804 A	$2.10^{+0.19}_{-0.18}$	$1.45^{+0.85}_{-0.71}$	13.8	**99.9%**

Notes. Significance levels above 99% confidence according to the F-test are in boldface, corresponding to the spectra actually requiring extra absorption. Column 1: ObsID and image; Col. 2: photon index; Col. 3: column density in excess of the Galactic value (in units of 10^{22} cm^{-2} and placed at $z = 1.695$); Col. 4: $\Delta\chi^2$ compared to Model pl (Δdof = 1); Col. 5: F-test confidence level. All the errors are computed at a 90% confidence level for one parameter of interest.

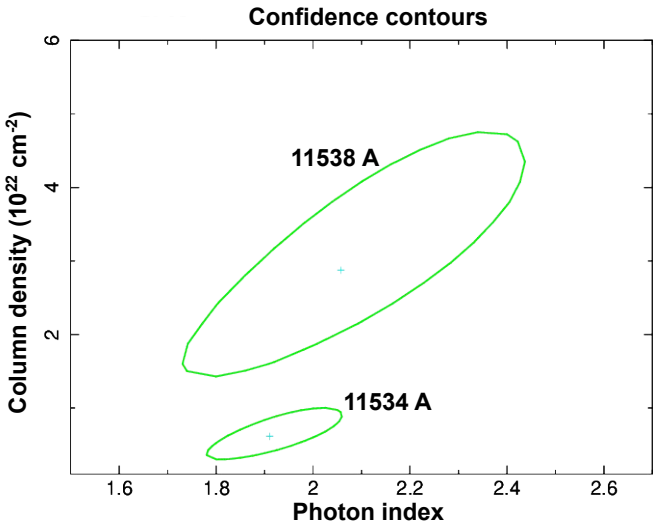

Fig. 5. 90% confidence contours of $N_{\rm H}$ vs. Γ for ObsIDs 11534 A and 11538 A. These correspond to the spectra that show the largest difference in column density, among the four that require a cold absorber at more than a 99% confidence level.

3.2. Narrow emission and absorption features

We next searched for emission and absorption features, again only in the HSS spectra to obtain better constraints. A first blind search was carried out by applying the method developed by Tombesi et al. (2010). Stepping both the energy and the normalization of a Gaussian component over the entire spectral range, this method allowed us to visualize the statistical improvement ($\Delta\chi^2$ for two parameters) produced by the addition of a narrow feature ($\sigma = 0.01$ keV) in terms of energy versus normalization confidence contours over the whole energy range. We then built the best-fit models of all the HSS spectra by adding a Gaussian component for each emission and absorption line indicated at more than a 90% confidence level by the blind search. Even though it is known to be unreliable when assessing the significance of narrow features (Protassov et al. 2002), we computed the F-test significance for each line to have a slightly better constraint than that of the blind search and only kept those features that are still above a 90% confidence level. Finally, we evaluated the actual significance of the absorption lines at $E_{\rm rf} > 7$ keV by building a Bayesian posterior predictive probability distribution through Monte Carlo simulations, as argued for by Protassov et al. (2002).

We applied the Tombesi et al. (2010) tool over the 0.4–5.0 keV observed-energy range (~1–13 keV rest-frame energy band), which corresponds to the range of interest for both soft X-ray features and iron resonant lines. The upper energy limit

Table 4. Rest-frame energies and equivalent widths of (a) the emission and (b) the absorption lines detected at more than 90% confidence in the high-statistics sample, based on the F-test.

(a) Emission lines				
ObsID	$E_{\rm line}$	EW	Cont.	F-test
431 A	$5.90^{+0.31}_{-0.36}$	368^{+277}_{-278}	90%	90.4%
11534 A	$3.65^{+0.13}_{-0.10}$	101^{+69}_{-68}	90%	93%
	$5.35^{+0.13}_{-0.12}$	179^{+111}_{-111}	90%	93%
11534 D	$2.25^{+0.10}_{-0.10}$	163^{+137}_{-107}	90%	98.5%
12831 A	$4.04^{+0.14}_{-0.15}$	75^{+57}_{-57}	90%	93%
	$6.47^{+0.11}_{-0.12}$	284^{+148}_{-148}	99%	**99.7%**
13961 A	$3.78^{+0.16}_{-0.12}$	173^{+105}_{-105}	90%	96%
(b) Absorption lines				
ObsID	$E_{\rm line}$	EW	Cont.	F-test	MC
431 A	$11.92^{+0.23}_{-1.69}$	1181^{+778}_{-575}	99%	99.5%	**99.5%**
11534 A	$8.01^{+0.42}_{-0.14}$	287^{+212}_{-185}	90%	97%	90.3%
12831 A	$9.78^{+0.43}_{-0.18}$	255^{+211}_{-169}	90%	95%	84.2%
	$10.90^{+0.53}_{-0.20}$	368^{+258}_{-196}	99%	99.1%	94.9%
13961 A	$9.39^{+1.90}_{-0.08}$	1025^{+542}_{-532}	99%	98.3%	**99.1%**
14514 A	$12.51^{+0.10}_{-2.28}$	1861^{+1354}_{-1273}	90%	92%	98.4%

Notes. Significance levels above 99% confidence, according to the F-test in (a) and according to Monte Carlo simulations in (b), are reported in boldface. Column 1: ObsID and image; Col. 2: line energy (in units of keV); Col. 3: line rest-frame equivalent width (in units of eV); Col. 4: blind-search confidence level; Col. 5: F-test confidence level; Col. 6: Monte-Carlo-simulation confidence level. All the errors are computed at a 90% confidence level for one parameter of interest. The energy width of the lines is set to 0.01 keV.

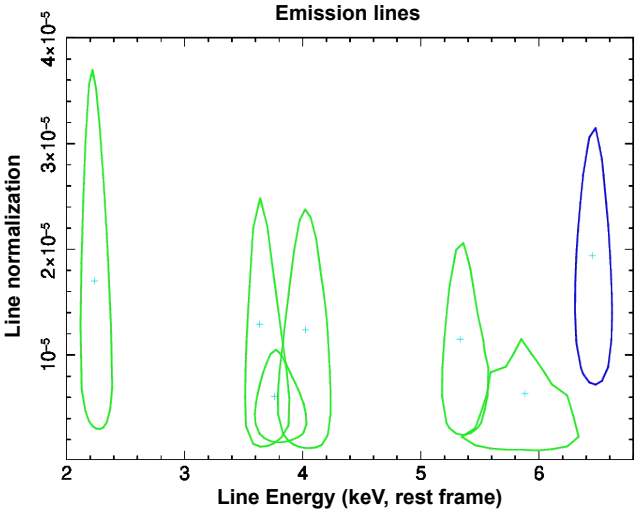

Fig. 6. 90% energy-normalization confidence contours (1.6σ) for the emission lines reported in Table 4a (ObsIDs 431 A, 11534 A, 11534 D, 12831 A, 13961 A). The blue contour corresponds to the line detected at more than a 99% confidence level in ObsID 12831 A (based on the F-test significance).

was set to exclude the bins with the lowest S/N. We selected as baseline models either Model pl or Model pl_a based on the requirement of extra absorption (see Table 3).

We then obtained the best-fit models by adding a narrow `zgauss` component for each line indicated at a confidence above 90% from the blind search. We only kept those lines with a significance above 90% confidence both from the blind search and the F-test; these are summarized in Table 4. This procedure indicated the presence (at a 90% confidence level) of blueshifted iron resonant absorption lines in 5 spectra out of 14.

Finally, through Monte Carlo simulations we evaluated the actual significance of the absorption lines in Table 4b. Following Protassov et al. (2002), each of these 5 spectra was simulated 1000 times through the `XSPEC` `fakeit` function from the respective null model (Model pl or Model pl_a if extra absorption was required – see Table 3). This confirmed that all the absorption lines at $E_{\rm rf} > 7$ keV are detected above 90% confidence except the one at 9.8 keV in ObsID 12831 A (see Table 4b). Thus, we find blueshifted iron resonant absorption lines in 5 epochs out of the 11 included in the HSS. Through the binomial distribution, we then evaluated the global probability of detecting these absorption lines in 5 spectra out of a sample of 14 by chance. We conservatively considered all the lines as detected at 90% confidence, even though more than half show higher significance. The probability of a by-chance detection is $P = 7.76 \times 10^{-3}$, yielding an overall significance of 99.2% (i.e., slightly below 3σ) for the detection of these absorption lines at $E_{\rm rf} > 7$ keV throughout the HSS. To inspect the persistence of such features through the different epochs, we overlapped the 1.6σ confidence contours of the narrow emission and absorption lines separately (Figs. 6 and 7, respectively).

The emission lines (Fig. 6) span over the 2.2–6.5 keV rest-frame energy band. The microlensed Fe Kα line found by Dai et al. (2003) in the combined spectra of ObsIDs 431 A and 1632 A ($E = 5.7^{+0.2}_{-0.3}$ keV, $\sigma = 0.87^{-0.30}_{-0.15}$ keV) is only marginally detected (90% confidence) in the spectrum of ObsID 431 A as a narrow line, probably due to the fact that we are analyzing single-epoch spectra while Dai et al. (2003) stacked the first two observations. The energy of the highly significant emission line in ObsID 12831 A ($E_{\rm rf} = 6.47^{+0.11}_{-0.12}$ keV) is consistent, within 1.6σ errors, with the centroid energy of the skewed line found by Reynolds et al. (2014) ($E = 6.58 \pm 0.03$ keV) in the combined spectra of all the images, stacking the first 26 observations (ObsIDs 431–14514). Following Dai et al. (2003) and Chartas et al. (2016a, 2017), the remaining emission lines can be associated with microlensed Fe Kα lines.

The absorption features (Fig. 7) show a group of values around 11 keV and one line at about 8 keV. Each of the confidence contours of the lines clustered around 11 keV cover a wide range of energy. This could be interpreted as being due to the blend of two or more lines given the lower S/N at the higher energies, thus larger energy bins, or ascribed to intrinsic very broad lines as seen in other high-z lensed and unlensed quasars, for instance APM 08279+5255 (Chartas et al. 2009) and HS 1700+6416 (Lanzuisi et al. 2012). By letting the width of the absorption lines in Table 4b free to vary, we found them to be consistent with zero, with upper limits ranging from 0.8 keV (ObsID 12831 A) up to 3.2 keV (ObsID 13961). The feature in ObsID 13961 A is the most peculiar; an intrinsically broad ($\sigma = 2.2^{+1.0}_{-0.5}$ keV) line would yield a better fit but the low statistics prevent us from simultaneously constraining the three line parameters (energy, width, normalization). As a result, we consider all the lines in Table 4b as consistent with being narrow.

The highly significant absorption lines (blue contours in Fig. 7) are both found at energies above 9 keV (rest frame) and are consistent with each other at 1.6σ. These features are detected in observations 431 and 13961, which are separated by twelve years (~4.5 yr proper time), and are also consistent

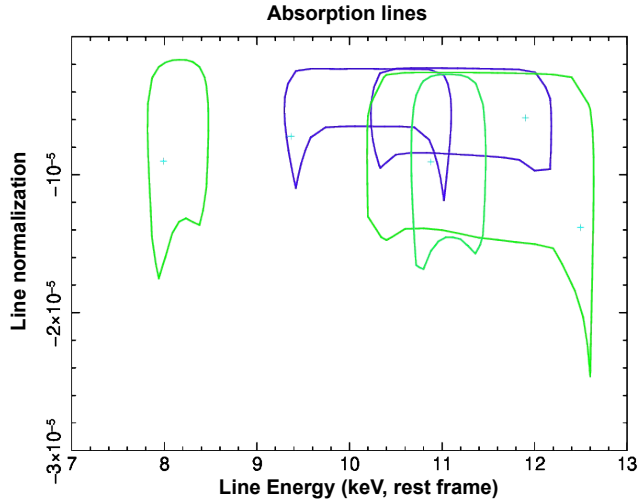

Fig. 7. 90% energy-normalization confidence contours (1.6σ) for the absorption lines reported in Table 4b (ObsIDs 431 A, 11534 A, 12831 A, 13961 A, 14514 A). Those in blue correspond to the lines detected at more than a 99% confidence level (based on the Monte-Carlo-simulation significance).

in energy with the slightly less significant features of ObsIDs 12831 and 14514. Thus, we infer that the lines at $E_{\rm rf} >$ 9 keV are presumably produced by the same highly ionized outflow which, from the period elapsed between the observations, is most likely variable. Interestingly, there seems to be no clear correlation between the additional absorption found in Sect. 3.1 and the detection of these absorption lines above 7 keV. In fact, only one spectrum (ObsIDs 11534 A) out of the four requiring an additional cold absorber presents such lines above 90% confidence.

Finally, we analyzed the combined spectra of images B+C+D from ObsIDs 431, 12831, and 13961, which are those observations in which image A shows highly significant absorption and/or emission lines (see Tables 4a and b). In the absence of microlensing events, since the time delays between the images are short when compared to the intrinsic variability timescale, one would expect the B+C+D combined spectra to show the same kind of features as the image A spectra at a confidence at least higher than 90%, since the number of counts of the stacked spectra is similar to that of the respective image A. We find that the B+C+D spectra do not present any of the lines of Tables 4a and b at more than 90% confidence. However, the upper limits we derive on their equivalent widths (EWs) are consistent with those of the respective image A lines. Our interpretation is that one, or more than one, of images B, C, and D is microlensed, thus the absorption lines are smeared out in the individual image spectra and the Fe Kα emission lines are likely blueshifted or redshifted, becoming even more diluted when we stack the images together.

3.3. Summary of the Chandra spectral results

We find clear spectral index variability at a significance larger than 99% as inferred from the analysis of the whole *Chandra* dataset (Fig. 3). From the Γ ratios, those variations seem to be intrinsic and not induced by microlensing. Photon-index variability might also be induced by variable absorption in some observations, as the HSS analysis pointed out (Table 3). Having a variability timescale of ~0.3 yr (rest frame), such an absorber is most likely dominated by an in situ component.

Five spectra of the HSS also show narrow emission lines below 3.5 keV in the observed frame (significance above 90% confidence – Table 4a). In one spectrum (ObsID 12831 A) we detect a highly significant narrow emission line at $E_{\rm rf} = 6.47^{+0.11}_{-0.12}$ keV; this energy is consistent with that detected by Reynolds et al. (2014). The line found by Dai et al. (2003) is only marginally detected in the spectrum of ObsID 431 A.

Finally, five spectra show narrow absorption features in the 3–5 keV observed-frame energy band (~8–13.5 keV rest frame) at more than 90% confidence (assessed through Monte Carlo simulations – Table 4b). A certain recurrence and/or persistence of those features in this energy range is indicated by the consistency of their confidence contours (Fig. 7), although we note that the error associated with the energy of the lines is typically large. The overall significance of detecting such features in the HSS is proved to be almost 3σ.

4. *XMM-Newton* spectral analysis

Having assessed the source spectral variability and the presence of spectral complexities through the *Chandra* observations, we then analyzed the *XMM-Newton* spectra, and attempted to model those complexities with reflection and complex absorption models. Both XMM 2002 and XMM 2018 spectra were grouped in order to obtain at least 20 counts per bin. Given the large number of counts (Table 2), we set the minimum energy width of each bin at one third of the CCD resolution using the task `specgroup` within SAS 16.1, so as not to oversample the energy resolution of the instrument. Due to background-dominated bins at the higher energies, the spectral fitting of XMM 2002 and XMM 2018 data was performed in the 0.3–8 keV observed-energy range (0.8–22 keV rest-frame energy range) and in the 0.3–7.0 keV observed-energy range (1–19 keV rest-frame energy range), respectively, to obtain more reliable results. For both observations, we analyze and report here only the EPIC-pn spectra, which deliver the best S/N, but our results were also compared and confirmed by checking their consistency with the EPIC-MOS data.

4.1. XMM 2002

The observed-frame best-fit residuals to Model `pl` (Fig. 8, panel b and Table 5) show clear spectral complexities throughout the whole energy band. Those that stand out are a deficit of counts at ~2.7 keV ($E_{\rm rf} \sim$ 7.4 keV) and at ~4.4 keV ($E_{\rm rf} \sim$ 11.8 keV), the latter being consistent with the majority of those found in the *Chandra* spectra. Moreover, an excess of counts at ~2.1 keV ($E_{\rm rf} \sim$ 5.7 keV) and signatures of absorption in the soft band below ~0.6 keV ($E_{\rm rf} \sim$ 1.6 keV) are also present.

Based on the results obtained from the *Chandra* observations, we investigated the need for an extra cold absorber at the quasar's redshift, either uniformly or partially covering the source (Model `pl_a=phabs*zphabs*zpo`; and Model `pl_pca=phabs*zpcf*zpo`, respectively; best-fit parameters in Table 5). The data do require extra absorption at the quasar redshift and are slightly better ($\Delta\chi^2 \sim 6$ for one additional parameter) reproduced by a partial covering medium. By adding a narrow Gaussian component to Model `pl_pca` for each of the narrow features hinted at by the residuals in Fig. 8 (panel b), the two in absorption turn out to be required by the data ($\Delta\chi^2 > 10$ for the addition of two parameters, each), while the emission line is only marginally detected (90% confidence).

Following Protassov et al. (2002), we evaluated the actual significance of the two narrow absorption features through

Table 5. Summary of the best-fit parameters for each model tested for XMM 2002 data.

Model	Γ	$N_{\rm H}$	CF	$\log\xi$	$z_{\rm abs}$	R	$E_{\rm e.l.}$	$\Delta\chi^2$	$\Delta\nu$	$\chi^2_r\,(\nu)$
pl	1.66 ± 0.04	–	–	–	–	–	–	–	–	1.56 (85)
pl_a	1.82 ± 0.07	0.32 ± 0.12	–	–	1.695	–	–	22.6	1	1.31 (84)
pl_pca	1.91 ± 0.11	$2.1^{+1.4}_{-1.2}$	$0.50^{+0.10}_{-0.12}$	–	1.695	–	–	28.9	2	1.25 (83)
pl_wa	1.74 ± 0.04	$28.2^{+1.4}_{-1.8}$	–	$2.5^{+0.1}_{-0.3}$	$\simeq$1.445	–	–	34.1	3	1.20 (82)
pl_pca_pex_el	2.57 ± 0.32	$2.3^{+0.7}_{-0.7}$	$0.74^{+0.07}_{-0.11}$	–	1.695	$0.58^{+0.40}_{-0.27}$	$5.7^{+0.2}_{-0.2}$	54.2	5	0.98 (80)
pl19_pca_pex_el	1.90	$1.1^{+1.0}_{-0.8}$	$0.51^{+0.44}_{-0.12}$	–	1.695	<0.18	$5.7^{+0.2}_{-0.2}$	41.1	4	1.13 (81)

Notes. The fitting was carried out over the 0.3–8 keV observed-energy range because the data are background dominated above 8 keV. Column 1: Model name; Col. 2: photon index; Col. 3: column density in excess of the Galactic value (units of 10^{22} cm^{-2}); Col. 4: covering fraction of the extra absorption; Col. 5: logarithm of the extra-absorption ionization parameter (erg s^{-1} cm); Col. 6: observed redshift of the extra absorption; Col. 7: reflection scaling factor; Col. 8: energy of the emission line (units of keV); Cols. 9 and 10: $\Delta\chi^2$, $\Delta\nu$ compared to Model pl ($\chi^2 = 132.6, \nu = 85$); Col. 11: χ^2_r. The energy width of the emission line is set to 0.01 keV. All the errors are computed at a 90% confidence level for one parameter of interest. Model list: Model pl = `phabs*zpo`; Model pl_a = `phabs*zphabs*zpo`; Model pl_pca = `phabs*zpcf*zpo`; Model pl_wa = `phabs*warmabs*zpo`; Model pl_pca_pex_el = `phabs*zpcf*(zpo+pexrav+zgauss)`; Model pl19_pca_pex_el = `phabs*zpcf*(zpo+pexrav+zgauss)` with $\Gamma = 1.9$. All the models include Galactic absorption ($N_{\rm H} = 5.1 \times 10^{20}$ cm^{-2}).

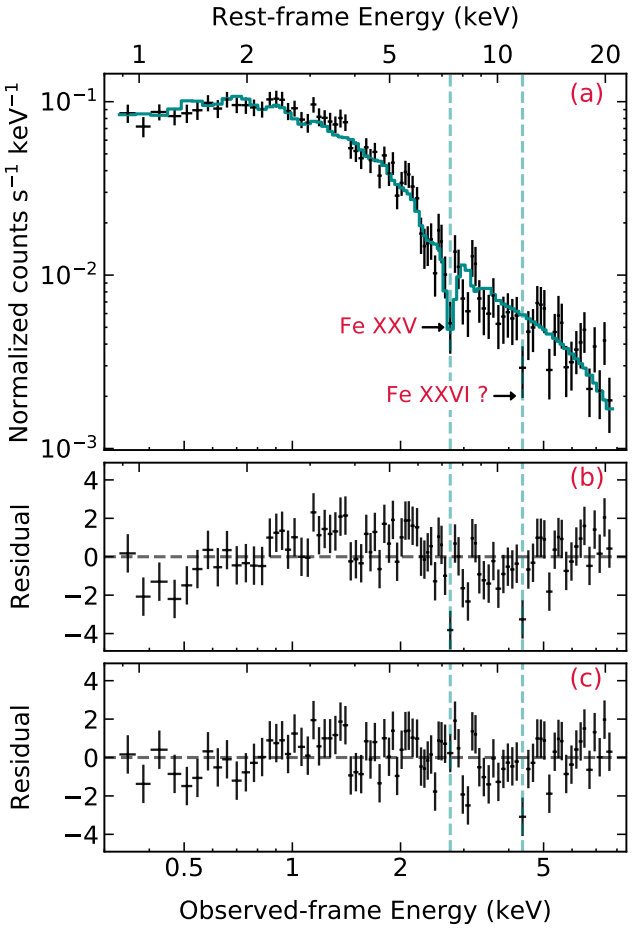

Fig. 8. XMM 2002 EPIC-pn spectrum of Q2237. *Panel a*: XMM 2002 data (black) and best-fit model (solid blue line) with Model pl_wa. The dashed blue lines indicate the UFO signatures. *Panel b*: XMM 2002 best-fit residuals for Model pl. *Panel c*: XMM 2002 best-fit residuals for Model pl_wa. The latter model self-consistently accounts for the absorption line at $E_{\rm rf} \simeq 7.4$ keV. The data are grouped to obtain at least 20 cts/bin, with the minimum energy width set to one third of the CCD energy resolution. The best-fit parameters are summarized in Table 5. Due to background-dominated bins above 8.0 keV, we restricted the fitting to the 0.3–8 keV observed-energy range (0.8–22 keV rest-frame energy range).

Monte Carlo simulations, as follows. To obtain the null models, we started from Model pl_pca plus the three narrow Gaussian components; the absorption line whose actual significance was to be measured was then deleted before performing the simulations. For each of the two null models, we simulated 1000 spectra through the `fakeit` function in `Xspec`. The two absorption lines turn out to be detected at $E_{\rm rf} = 7.4$ keV and $E_{\rm rf} = 11.8$ keV at confidence levels of 97.9% and 87%, respectively.

Given their energies, they are likely blueshifted iron resonant lines, thus produced by a (highly) ionized and outflowing material. To test this scenario, we decided to use `warmabs` (Kallman & Bautista 2001), an analytic XSTAR model for self-consistent ionized absorption (Model pl_wa= `phabs*warmabs*zpo`), which also takes into account the production of absorption lines. Based on the results for measurements in other high-z lensed quasars (Chartas et al., in prep.), we assumed solar abundances and a gas turbulent velocity of 5000 km s^{-1}, letting the column density ($N_{\rm H}$), the ionization parameter ($\log\xi$), and the redshift of the absorber ($z_{\rm o}$) vary. The `warmabs` model assumes that the AGN emission modeled in `Xspec` is the same radiation that illuminates and ionizes the absorber. The initial conditions (abundances and density) of the medium are loaded through a population file, which depends on the power-law slope of the illuminating radiation. To find the best-fit Γ, we created different population files ($n = 4 \times 10^4$ cm^{-3}, $v_{\rm turb} = 5000$ km s^{-1}) until the incident-radiation and the best-fit power-law photon indexes converged (within the errors). Model pl_wa yielded the best description of the XMM 2002 data ($\chi^2_r = 1.20$) and best-fit parameters for the ionized absorber of $N_{\rm H} = 2.8 \pm 0.2 \times 10^{23}$ cm^{-2}, $\log\left(\xi/{\rm erg\,s^{-1}\,cm}\right) = 2.5^{+0.1}_{-0.3}$, and $z_{\rm o} \simeq 1.445$ (see Table 5 and Fig. 8, panels a and c). The observed value $z_{\rm o}$ of the absorber redshift is related to the intrinsic redshift $z_{\rm a}$ of the medium (i.e., in the source rest frame) as $(1 + z_{\rm o}) = (1 + z_{\rm a})\left(1 + z_{\rm q}\right)$. Thus, the outflow velocity $v_{\rm out}$ can be determined from the relativistic Doppler effect formula $1 + z_{\rm a} = \sqrt{(1-\beta)/(1+\beta)}$, where $\beta = v_{\rm out}/c$. Given $z_{\rm q} = 1.695$, the outflow velocity corresponding to $z_{\rm o} \simeq 1.444$ is $v_{\rm out} = 0.10 \pm 0.01c$. This ionized wind model naturally explains both the structure in the soft band and the absorption feature at $E_{\rm rf} \simeq 7.4$ keV (Fig. 8), as opposed to the absorber of Model pl_pca, which, being cold, cannot be the origin of such a line. Given the wind ionization state and the

outflow velocity, this line is consistent with being dominated by Fe XXV, which has a rest-frame energy at rest of 6.7 keV. However, this same model fails to account for the second absorption line at $E_{\rm rf} \simeq 11.8$ keV (4.4 keV observed frame, see Fig. 8, panels a and c). Moreover, the narrow emission line at $E_{\rm rf} = 5.7 \pm 0.2$ keV is only marginally detected (90% confidence) when adding a Gaussian component to Model pl_wa. Its energy is consistent with that of the line we find in *Chandra* ObsID 431 A and with that of the microlensed Fe Kα found by Dai et al. (2003). Its width ($\sigma < 0.01$ keV), however, is not consistent with the broad one found by Dai et al. (2003) ($\sigma = 0.87^{+0.30}_{-0.15}$ keV). The results of Fedorova et al. (2008), who analyzed the XMM 2002 observation, tentatively detecting an emission line at $E_{\rm rf} = 6.0^{+0.7}_{-1.0}$ keV observed frame with an energy-width upper limit of $\sigma < 0.9$ keV, are consistent with ours.

Finally, we stress that the significance obtained for the 7.4 keV absorption line through the Monte Carlo simulations does not correspond to that of the UFO. In fact, assessing the F-test significance of the `warmabs` component leads to a detection of the outflow that is well above the 99.99% confidence level. This is linked to the fact that the UFO not only explains the absorption line by itself but also acts on the shape of the soft-band continuum, as the two lower panels of Fig. 8 show.

For the sake of completeness, we also tested a reflection scenario. Instead of self-consistent reflection models that bind the Fe Kα line to the 6.4–6.7 keV range, we built a phenomenological model to let the emission line be placed at lower energies (Model pl_pca_pex_el= `phabs*zpcf*(zpo+pexrav+zgauss)`). The reflected-power-law photon index was set to that of the intrinsic emission, the abundances equal to solar, the inclination angle to 60°, the cutoff energy to 300 keV, and the reflection fraction to be negative, so as to only model the reflected emission through the `pexrav` component. The best-fit reflection fraction and photon index (Table 5) are $R = 0.58^{+0.40}_{-0.27}$ and $\Gamma = 2.57 \pm 0.32$ ($\chi^2_r = 0.98$), which corresponds to a considerably steeper power law, at the limits of the expected values for an AGN (e.g., Perola et al. 2002; Piconcelli et al. 2005). In this case, the emission line is detected at $E_{\rm rf} = 5.7 \pm 0.2$ keV above 99% confidence as a narrow line, with an EW of EW = 154^{+99}_{-103} eV. Following Makishima (1986), this agrees with what is expected given the column density. However, this model is almost in tension with Leahy (2001) concerning the reflection fraction R. The steep power law may be caused by the known photon index–column density degeneracy. Therefore, we tried setting the photon index (Model pl19_pca_pex_el) to the standard value $\Gamma = 1.90$ for high-z quasars (e.g., Vignali et al. 2005; Just et al. 2007), which is also consistent with the average Γ of the *Chandra* HSS and that of the absorption models for this spectrum (see Table 5). When doing so, the reflection fraction becomes consistent with zero (90% confidence upper limit: $R < 0.18$) and the quality of the fit decreases ($\chi^2_r = 1.13$). Therefore, the reflection component turns out not to be physically, in the first case, or statistically, in the second case, required by the 2002 data, confirming earlier results by Fedorova et al. (2008).

4.2. XMM 2018

As for the other spectra, we began our analysis of the XMM 2018 EPIC-pn spectrum by inspecting the best-fit residuals to Model pl (Fig. 9, panel b, Table 6). Due to background-dominated bins above 7 keV, we restricted the fitting to the 0.3–7 keV observed-energy range (1–19 keV rest-frame energy range). The residuals (Fig. 9, panel b) show complexities in the soft-energy band that are likely due to an absorber and indicate a prominent emission line just below 3 keV in the observed frame. At higher energies, however, the distribution is quite flat, although noisy, suggesting the absence of a significant reflection component. No hints of absorption lines in the hard-energy band are seen either.

Using the same logical steps as for XMM 2002, we started by adding more complex absorption models to fit the low energy continuum. All the best-fit parameters of the tested models are summarized in Table 6. Given the shape of the residuals, the absorber during this observation could either be cold and partially covering the emitting source, or ionized (Model pl_pca and Model pl_wa[3], respectively). For completeness, we also investigated the case of a cold medium blocking all the intrinsic emission (Model pl_a) which, as expected, turned out not to be required by the data. In all three cases, we set the absorber's redshift to the systemic of the quasar, based on the results obtained with the *Chandra* data (Sect. 3.1) and because no absorption lines above 7 keV rest-frame were found (i.e., there are no hints of outflowing material). When limiting the analysis to one feasible absorption component, the XMM 2018 spectrum is best reproduced by a power-law emission modified by a partial covering medium (Model pl_pca, see Table 6). The prominent emission line indicated by the residuals (Fig. 9, panel b) is found to be narrow (Model pl_pca_el, Table 6 and Fig. 9, panels a and c) with a 90% energy-width upper limit of $\sigma < 0.53$ keV. Thus for XMM 2018 we find a rather thick absorber that blocks part of the intrinsic emission ($N_{\rm H} \simeq 1.0 \times 10^{23}$ cm^{-2}, CF $\simeq 0.53$) and a significant emission line with a rest-frame energy and EW of $E_{\rm rf} = 6.84 \pm 0.11$ keV and EW = 267 ± 111 eV. The energy is inconsistent with both that of the marginal detection in the 2002 data (see Sect. 4.1) and that of the skewed emission line found by Reynolds et al. (2014). To see whether the production of this line could be ascribed to the absorber, we evaluated the upper limit of the medium ionization state through the `warmabs` model. To mimic the partial absorption of the intrinsic emission, we included two power-law plus emission-line components, the first seen directly and the other as scattered by the absorber (Model pl_pcwa=`phabs*[(zpo+zga)+warmabs*(zpo+zga)]`), both modified by Galactic absorption. The slopes and the line parameters of the two terms were linked to each other, since the primary emission is the same for both components. We inferred a 90% upper limit to the ionization parameter of $\log\left(\xi/{\rm erg\,s^{-1}\,cm}\right) = 2.2$ and a covering fraction CF = 0.58 ± 0.33, which is consistent with that obtained with Model pl_pca (Table 6). The inferred ionized state is not consistent with that of the UFO detected in XMM 2002, and nor are the column densities. Thus, it is unlikely that the two absorbers are the same gas that changed in covering fraction.

Following Makishima (1986), the absorber ionization state ($\log\left(\xi/{\rm erg\,s^{-1}\,cm}\right) \leq 2.2$) translates into a medium that is dominated by iron from Fe I to Fe XX, while, from its energy, the line we detect is consistent with being dominated by Fe XXV–XXVI. Thus, this feature cannot be produced by the absorber itself since it would require a much more ionized gas ($\log\left(\xi/{\rm erg\,s^{-1}\,cm}\right) \geq 3.0$). Unfortunately, we are not able to verify whether an additional highly ionized medium could be required by the data because the S/N of the present data does not allow us to constrain such a complex model. Another possible explanation for the 6.8 keV line could be the microlensing differential magnification of a relativistic blurred Fe Kα produced by

[3] Chemical abundances and the gas turbulent velocity were set as for XMM 2002 (see Sect. 4.1). The best-fit Γ was found using the same method as for XMM 2002.

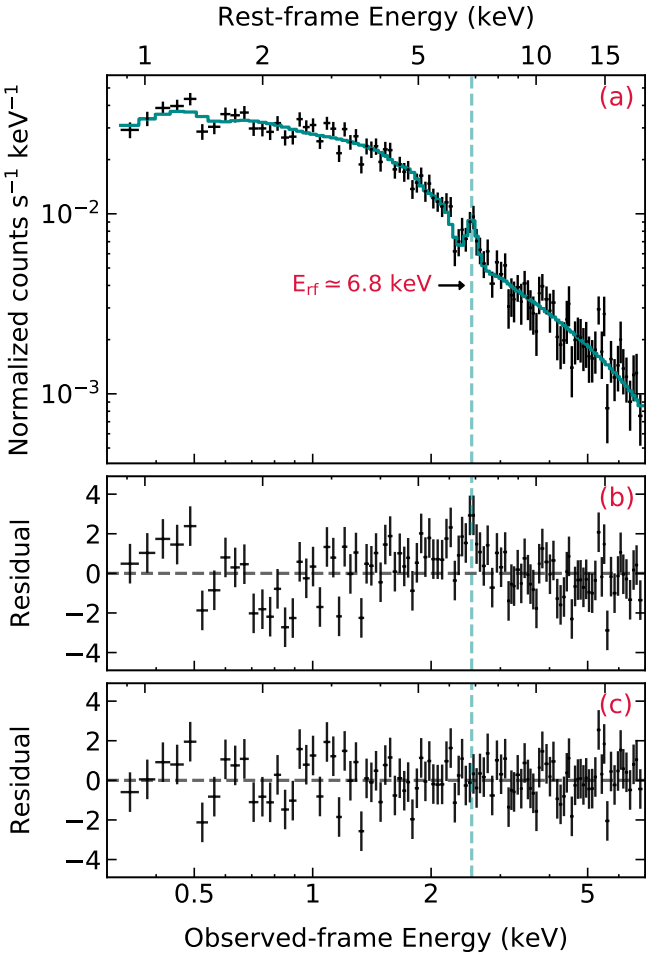

Fig. 9. XMM 2018 EPIC-pn spectrum of Q2237. *Panel a*: XMM 2018 data (black) and best-fit model (solid blue line) with Model pl_pca_el. The dashed blue line indicates the emission line at $E_{rf} = 6.84 \pm 0.11$ keV. *Panel b*: XMM 2018 best-fit residuals for Model pl. *Panel c*: XMM 2018 best-fit residuals for Model pl_pca_el. The data are grouped to obtain at least 20 cts/bin, with the minimum energy width set to one third of the CCD energy resolution. The best-fit parameters are summarized in Table 6. Due to background-dominated bins above 7.0 keV, we restricted the fitting to the 0.3–7.0 keV observed-energy range (1–19 keV rest-frame energy range).

the Compton reflection in the accretion disk, as proposed in other sources by Chartas et al. (2016b, 2017). Based on this argument, we tested whether a reflection scenario would give a better representation of the XMM 2018 data, using the same phenomenological model discussed in Sect. 4.1 (Model pl_pca_pex_el). This model returns a best fit that on a statistical basis is as good as that of Model pl_pca, but its reflection fraction R is consistent with zero at the 90% confidence level ($R \leq 0.16$, see Table 6). On the one hand, this result confirms that the Compton reflection is not a dominant component in the Einstein Cross emission but, on the other hand, it does not completely rule out the interpretation of the 6.8 keV emission line as a microlensed Fe Kα line. Standard reflection models, like `pexrav`, assume the reflection continuum as produced by the whole disk. In the case of a microlensing event magnifying the inner regions of the approaching side of the accretion disk, Popović et al. (2006) demonstrate that only the emission associated to the blueshifted part of the Fe Kα line is enhanced, while the reflection continuum is not, unless the microlensing event is monitored for its whole duration. Since the source crossing time in the Einstein Cross is estimated to be a few months (Mosquera & Kochanek 2011), we cannot rule out the possibility of this emission line being a microlensed Fe Kα.

4.3. Summary of the XMM-Newton results

The XMM 2002 spectra are best physically and statistically reproduced by a complex absorber with $N_H \simeq 2 \times 10^{23} \mathrm{cm}^{-2}$, $\log\left(\xi/\mathrm{erg\,s^{-1}\,cm}\right) \simeq 3.0$, and outflow velocity of $v_{out} \sim 0.1c$, typical of UFOs. This also explains the prominent absorption iron resonant line measured at $E_{rf} \simeq 7.4$ keV and interpreted as Fe XXV.

The 2018 data do not show any similar blueshifted absorption features and are best fitted by a partially covering, mildly ionized material, with $N_H \simeq 1.0 \times 10^{23}$ cm^{-2}, CF $\simeq 0.53$ and with a 90% ionization-state upper limit of $\log\left(\xi/\mathrm{erg\,s^{-1}\,cm}\right) < 2.2$. We detect a significant narrow emission line at $E_{rf} = 6.84 \pm 0.11$ keV, with an EW of EW $= 267 \pm 111$ eV. This line is inconsistent with being produced by the absorber itself because, given its energy, a much more ionized medium would be required.

Constraining the reflection component is challenging for both the XMM spectra, also due to the limited energy range provided at high energies. We find that for the 2002 data, a reflection component is statistically significant only when a very steep power law ($\Gamma \simeq 2.65$) is assumed, while it is negligible when a typical AGN slope ($\Gamma \simeq 1.9$) is adopted. Regarding the 2018 data, despite the presence of a prominent emission line at $E_{rf} = 6.84 \pm 0.11$ keV, a reflection component is found not to be statistically required.

5. Discussion and results

We have presented the results obtained from the analysis of all the available X-ray data of the Einstein Cross (Q2237+030), a quasar at $z = 1.695$ that is gravitationally lensed in four images by a foreground spiral galaxy. We analyzed 40 archival observations, 37 taken by *Chandra* and 3 by *XMM-Newton*, covering a period of 18 years, for a total of ~0.9 Ms.

From the *Chandra* data, we probed the source spectral variability, using the photon-index variations through the epochs as proxy. These are qualitatively consistent across the four images (i.e., intrinsic), which supports the assumption made by Chen et al. (2012), who linked the photon index across the images when fitting spectra extracted from the same observation. To assess the origin of such variability, we limited the analysis to the HSS, which is made up of the 14 spectra extracted from 11 observations that show the highest number of counts (above 500 cts in the 0.4–7 keV observed-frame energy range); this allowed us to better constrain the model parameters. We find that an additional cold absorber is definitely required (above 99% confidence) in four of the HSS spectra, corresponding to three different epochs. Moreover, the column density is consistent with being variable at more than 99% confidence between the epochs. Thus, the spectral variability is likely ascribed to a variable absorber placed at the quasar's redshift, but we cannot exclude the possibility that part of it could be produced by the variation of the source intrinsic power-law emission as well.

The *XMM-Newton* data are fundamental in investigating the need for extra absorption and the nature of the medium, given the much higher counting statistics they provide. We find that the XMM 2002 data are consistent with a UFO scenario with $N_H = 2.0^{+0.6}_{-0.5} \times 10^{23}$ cm^{-2}, $\log\left(\xi/\mathrm{erg\,s^{-1}\,cm}\right) = 3.0 \pm 0.1$ and $v_{out} = 0.1 \pm 0.01c$, which explains the prominent absorption

Table 6. Summary of the best-fit parameters for each tested model for XMM 2018 EPIC-pn spectrum.

Model	Γ	$N_{\rm H}$	CF	logξ	$z_{\rm abs}$	R	$E_{\rm e.l.}$	$\Delta\chi^2$	$\Delta\nu$	χ^2_r (ν)
pl	1.56 ± 0.03	–	–	–	–	–	–	–	–	1.64 (102)
pl_a	1.56 ± 0.03	<0.04	–	–	1.695	–	–	−0.4	1	1.72 (101)
pl_pca	1.99 ± 0.10	$11.1^{+2.5}_{-2.2}$	0.56 ± 0.08	–	1.695	–	–	47.3	2	1.20 (100)
pl_pca_el	1.96 ± 0.10	$10.3^{+2.5}_{-2.2}$	0.53 ± 0.09	–	1.695	–	6.84 ± 0.11	62.4	4	1.07 (98)
pl_wa	1.62 ± 0.03	<0.19	–	$2.4^{+0.4}_{-0.6}$	1.695	–	–	2.1	2	1.65 (100)
pl_pca_pex_el	$2.03^{+0.20}_{-0.15}$	$9.4^{+3.0}_{-2.3}$	0.56 ± 0.09	–	1.695	<0.16	6.84 ± 0.10	63.7	5	1.07 (97)

Notes. The fitting was carried out over the 0.3–7 keV observed-energy range because the data are background dominated above 7 keV. Column 1: model name; Col. 2: photon index; Col. 3: column density in excess of the Galactic value (units of 10^{22} cm^{-2}); Col. 4: covering fraction of the extra absorption; Col. 5: logarithm of the extra-absorption ionization parameter (erg s^{-1} cm); Col. 6: observed redshift of the extra absorption; Col. 7: reflection scaling factor; Col. 8: energy of the narrow emission line (units of keV); Cols. 9 and 10: $\Delta\chi^2$, $\Delta\nu$ compared to Model pl ($\chi^2 = 167.4, \nu = 102$); Col. 11: χ^2_r. The energy width of the emission line is set to 0.01 keV. All the errors are computed at a 90% confidence level for one parameter of interest. Model list: Model pl = `phabs*zpo`; Model pl_a = `phabs*zphabs*zpo`; Model pl_pca = `phabs*zpcf*zpo`; Model pl_wa = `phabs*warmabs*zpo` with $z \equiv z_{\rm q}$; Model pl_pca_el = `phabs*zpcf*(zpo+zgauss)`; Model pl_pca_pex_el = `phabs*zpcf*(zpo+pexrav+zgauss)` with $\Gamma = 1.9$. All the models include the Galactic absorption ($N_{\rm H} = 5.1 \times 10^{20}$ cm^{-2}).

line at $E_{\rm rf} = 7.4 \pm 0.1$ keV. However, the same UFO cannot explain the second absorption line detected at ∼11.8 keV, unless we assume it to be the indicator of a blueshifted Fe XXVI Lyα ($E_{\rm rf} = 6.97$ keV at rest) produced by an even faster component outflowing at ∼0.5c. This would not be the first UFO showing more than one outflow component and at such extremely high velocities (see, for instance, the case of APM 08279+5255, Chartas et al. 2009).

The rest-frame absorption-corrected 2–10 keV luminosity of Q2237 during the 2002 observation is $L_{2-10} \simeq 6.6 \times 10^{45}$ erg s^{-1}. Given a magnification factor of $\mu \approx 16$ (Schmidt et al. 1998), the intrinsic absorption-corrected luminosity is $L^{\rm int}_{2-10} \simeq 4.1 \times 10^{44}$ erg s^{-1}. From the UV luminosity $\log(\lambda L_\lambda)_{1450\text{Å}} \simeq 45.53$ reported in Assef et al. (2011) and assuming a conversion factor of ≃4 (Richards et al. 2006), we find a bolometric luminosity of $L_{\rm bol} \simeq 1.4 \times 10^{46}$ erg s^{-1}. Based on Lusso et al. (2012) and the recent work by Duras et al. (2020), the predicted 2–10 keV intrinsic luminosity would be $L^{\rm int}_{2-10} \simeq 4 \times 10^{44}$ erg s^{-1}, which is in good agreement with the one we measure. Assef et al. (2011) estimate the black hole mass $M_{\rm BH}$ from the Hβ broadening to be $\log(M_{\rm BH}/M_\odot) = 9.08 \pm 0.39$, which leads to an Eddington luminosity of $L_{\rm Edd} \simeq 1.5 \times 10^{47}$ erg s^{-1} ($\lambda_{\rm Edd} \approx 0.1$).

Assuming the high significance of the outflow observed in XMM 2002 at $v_{\rm out} \simeq 0.1c$, we can derive the physical properties of the wind, by adopting standard "prescriptions" (e.g., Tombesi et al. 2012; Crenshaw & Kraemer 2012) and including the uncertainties on the best-fit parameters, so to place this detection in a broader context and compare it with the measurements in other QSOs at $z \geq 1.5$ and in the local Universe. Following Crenshaw & Kraemer (2012), the mass-outflow rate can be obtained using the formula $\dot{M}_{\rm out} = 4\pi r \mu m_{\rm p} N_{\rm H} v_{\rm out} C_{\rm g}$, where $m_{\rm p}$ is the proton mass, μ is the mean atomic mass per proton (1.4 for solar abundances), r is the distance from the BH, and $C_{\rm g}$ is the global covering factor of the wind. We assume $C_{\rm g} \approx 0.5$, based on the statistical study carried out by Tombesi et al. (2010), and recently confirmed by Igo et al. (2020), over a sample of local Seyfert galaxies. Moreover, we conservatively assume the outflow to be detected at the minimum distance from the BH, where the observed velocity $v_{\rm out}$ equals the escape velocity from the BH potential well, thus $r_{\rm min} = 2GM_{\rm BH}/v^2_{\rm out}$. We obtain $r_{\rm min} \approx 3.6 \times 10^{16}$ cm, which corresponds to ≃100 gravitational radii ($r_{\rm g} = GM_{\rm BH}/c^2$); considering the uncertainties on $M_{\rm BH}$, we find for $r_{\rm min}$ the range $r_{\rm min} \approx (0.9 - 7) \times 10^{16}$ cm. Using $r = r_{\rm min}$ as the radial location of the outflow, we estimate the lower limit to the following quantities. The mass outflow rate, given all the assumptions above, turns out to be $\dot{M}_{\rm out} \approx 5\, M_\odot$ yr^{-1}. Taking into account the 1σ uncertainties of the parameters, we find quite a wide range for the mass-outflow rate: $\dot{M}_{\rm out} \sim (0.6–10.3)\, M_\odot$ yr^{-1}. As a result, all the following quantities derived using $\dot{M}_{\rm out}$ will have likewise wide uncertainties. The outflow mechanical output ($\dot{E}_{\rm kin} = \frac{1}{2}\dot{M}_{\rm out} v^2_{\rm out}$) is $\dot{E}_{\rm kin} = 1.5 \times 10^{45}$ erg s^{-1}, which corresponds to an outflow efficiency of $\dot{E}_{\rm kin}/L_{\rm bol} \approx 0.1$. We obtain an outflow momentum rate of $\dot{p}_{\rm out} = \dot{M}_{\rm out} v_{\rm out} \approx 9.9 \times 10^{35}$ cm g s^{-2}, which is approximately twice the radiation pressure $\dot{p}_{\rm rad} = L_{\rm bol}/c$. Therefore, this UFO is consistent with generating efficient wind-driven AGN feedback that might indeed act on the evolution of the quasar host galaxy, given the $\dot{E}_{\rm kin}/L_{\rm bol} > 0.5\%$–$5\%$ threshold predicted by the models (e.g., Di Matteo et al. 2005; Hopkins & Elvis 2010). Moreover, since the outflow momentum rate is higher than $L_{\rm bol}/c$, magnetic forces might be playing a non-secondary role in accelerating this UFO. The derived wind parameters (column density, ionization state, and outflow velocity) are consistent with those of UFOs in local AGN (Tombesi et al. 2010) but the kinematic properties, albeit with wide uncertainties, seem to be higher than the average values for local objects (Tombesi et al. 2012). They are instead consistent with those of high-z AGN, for instance PID352 (Vignali et al. 2015), a bright, unlensed source at $z \approx 1.6$ that shows a similar $L_{\rm bol}$ (∼10^{46} erg s^{-1}). Furthermore, the properties of this UFO agree with the $v_{\rm out} - L_{\rm bol}$ and $L_{\rm bol} - \dot{E}_{\rm kin}$ relations in Fiore et al. (2017), computed for a compilation of local and (a small number of) high-redshift X-ray winds.

Interestingly, the XMM 2018 spectra do not show any absorption line in the hard band and seem to be best reproduced by a partially covering, mildly ionized absorber, with an ionization parameter of $\log\left(\xi/\text{erg s}^{-1}\text{ cm}\right) \leq 2.2$ (90% confidence limit). The intrinsic, absorption-corrected 2–10 keV luminosity for the 2018 observation is $L^{\rm int}_{2-10} \simeq 2.0 \times 10^{44}$ erg s^{-1}, approximately 49% of that found for the 2002 data. From the upper limit to the ionization state, we evaluated the lower limit to the absorber maximum distance from the central BH (being $\xi = L_{\rm X}/N_{\rm H} r_{\rm max}$): $r_{\rm max} \geq 4.7$ pc. Thus, it seems to be placed at a distance consistent with the typical range of the broad line region or the molecular torus (e.g., Jaffe et al. 2004; Burtscher et al. 2013).

Since accretion-disk winds are thought to have a global covering fraction less than unity, we propose a scenario where the wind has changed its direction with regard to the LOS and the disk between the two XMM observations, and part of the clouds contained within the molecular torus or the broad line region intercept the LOS during the second pointing. Given the short time elapsed, we think it is unlikely that the outflow has been totally suppressed between the two observations. Given that the *Chandra* observations were taken in between XMM 2002 and XMM 2018, we find that our statement is supported by the UFO signatures in the *Chandra* data. Moreover, the lowest timescale of the absorber variability obtained from *Chandra* HSS (≃0.3 yr rest frame) is linked to its distance from the central BH as $d \approx c\Delta t \approx 0.09$ pc, consistent with the innermost regions of the torus and of the broad line region, thus consistent with the proposed scenario (e.g., Perola et al. 2002; Risaliti et al. 2009; Burtscher et al. 2013). However, the lower statistics of the *Chandra* spectra prevent us from modeling the detected absorption lines with a physically accurate wind model producing them, that is, we are unable to investigate and constrain the presence of more complex absorbers than a neutral medium with the *Chandra* data.

In the *Chandra* HSS we find emission lines that span from ∼2.2 to ∼6.5 keV rest frame, which, following Dai et al. (2003) and Chartas et al. (2016b, 2017), might be interpreted as microlensed and relativistic Fe Kα lines. Moreover, the energy range they cover is consistent with the energies of the redshifted Fe Kα emission lines found by Chartas et al. (2016b) in RX J1131–1231. Interestingly, the only highly significant emission line is consistent with a regular Fe Kα line ($E_{\rm rf} = 6.47^{+0.11}_{-0.12}$ keV). Despite this fact, also this line seems to be microlensed since we do not detect it in the stacked spectrum of images B+C+D from the same observation. From a preliminary search for microlensing events in the *Chandra* multi-epoch light-curve ratios, there is no clear link between the observations in which we detect these emission lines and microlensing effects. In XMM 2018 we find a significant emission line at ≃6.8 keV that is inconsistent with being produced by the absorber, due to its ionization state. Even though a reflection component is not required by the data, such a line could be produced by a microlensing caustic that is crossing the inner regions of the accretion disk's approaching side. Such a microlensing event will lead to the magnification of blueshifted Fe Kα emission from a narrow inner region of the disk without magnifying the distant reflected continuum (Popović et al. 2006; Krawczynski & Chartas 2017; Krawczynski et al. 2019). The present data, however, do not allow us to verify either the presence of another highly ionized absorption component, since the data S/N is too low to constrain such a complex model, or the case of a microlensing event magnifying the inner regions of the accretion disk, since longer and less sparse *Chandra* monitoring would be required.

In the *Chandra* spectra, we detect, for the first time in this source, several blueshifted iron resonant absorption lines, with an overall significance slightly below 3σ. Interestingly, all the most significant lines (>99% confidence level) of the HSS (Table 4b) are grouped around the value of 11 keV and have energies consistent with the least significant (87% confidence level) feature of XMM 2002. If confirmed, they would imply a second and more extreme wind component with $v_{\rm out} \approx 0.3$–$0.5c$. Thus, the Einstein Cross could have experienced a multi-velocity UFO event, as found for other quasars, either nearby (e.g., PDS 456, Boissay-Malaquin et al. 2019; IRAS 00521–7054, Walton et al. 2019) or more distant (e.g., APM 08279+5255, Chartas et al. 2009).

Given the large number of X-ray observations of Q2237, for the first time ever we can roughly evaluate the wind duty cycle for a single high-z source. However, almost two thirds of the dataset did not provide a S/N high enough to constrain the presence or absence of the narrow features. In total, we detect UFO signatures at more than 90% confidence in 6 observations (5 from *Chandra*, 1 from *XMM-Newton*) out of the 13 analyzed to this purpose (11 from *Chandra*, 2 from *XMM-Newton*). Thus, we find the wind duty cycle to be $\mathrm{DC_w} \approx 0.46$ at 90% confidence. If we only consider those observations that show absorption lines at more than 95% confidence (3 from *Chandra*, 1 from *XMM-Newton*), the duty cycle turns out to be $\mathrm{DC_w} \approx 0.31$. Nonetheless, we cannot exclude the presence of UFO signatures that are too weak to be detected due to the too low S/N of the HSS spectra showing the least number of counts. For this reason, our estimates of $\mathrm{DC_w}$ represent the wind-duty-cycle lower limit over the 13 observations that provide data with high-enough statistics. Although strictly related to the S/N of the spectra, our estimation of this parameter represents the best we are able to achieve with present-day data.

With this work we add a new piece to the puzzle of high-redshift AGN ($z > 1.5$) that show complex spectra and sometimes show variable UFOs. So far, only around ten objects at $z \geq 1.5$ were analyzed to this purpose (of which only two are non-lensed quasars: HS 1700+6416, Lanzuisi et al. 2012; PID 352, Vignali et al. 2015), leading to a detection fraction of ∼70% (Chartas et al., in prep.). Expanding this high-redshift sample will be key in the future to better assess the occurrence and the properties of these events at the peak of the QSO activity. To this end, the launch of new-generation X-ray observatories (i.e., *Xrism* and *Athena*) will provide us with the means to obtain spectra with much higher S/N and spectral resolution with regard to those we can reach nowadays, essential ingredients in unveiling UFOs. This would allow us to better understand if and how disk-driven winds triggered efficient AGN feedback at the time when the scaling relations between SMBHs and host galaxies were put in place.

Acknowledgements. The authors thank the referee for the careful reading of the manuscript and the helpful comments. The authors also thank Gabriele Ponti for useful discussions. This work is based on observations obtained with *XMM-Newton*, an ESA science mission with instruments and contributions directly funded by ESA Member States and the USA (NASA). This research has made use of data obtained from the *Chandra* Data Archive, and software provided by the *Chandra* X-ray Center (CXC) in the application package CIAO. CV and MD acknowledge financial support from the Italian Space Agency (ASI) under the contracts ASI-INAF I/037/12/0 and ASI-INAF n.2017-14-H.0. BDM acknowledges support from the European Union's Horizon 2020 research and innovation programme under the Marie Skłodowska – Curie grant agreement No. 798726. MG is supported by the "Programa de Atracción de Talento" of the Comunidad de Madrid, grant No. 2018-T1/TIC-11733.

References

Assef, R. J., Denney, K. D., Kochanek, C. S., et al. 2011, ApJ, 742, 93
Boissay-Malaquin, R., Danehkar, A., Marshall, H. L., & Nowak, M. A. 2019, ApJ, 873, 29
Burtscher, L., Meisenheimer, K., Tristram, K. R. W., et al. 2013, A&A, 558, A149
Cappi, M., Tombesi, F., Bianchi, S., et al. 2009, A&A, 504, 401
Chartas, G., Brandt, W. N., & Gallagher, S. C. 2003, ApJ, 595, 85
Chartas, G., Eracleous, M., Dai, X., Agol, E., & Gallagher, S. 2007, ApJ, 661, 678
Chartas, G., Saez, C., Brandt, W. N., Giustini, M., & Garmire, G. P. 2009, ApJ, 706, 644
Chartas, G., Cappi, M., Hamann, F., et al. 2016a, ApJ, 824, 53
Chartas, G., Rhea, C., Kochanek, C., et al. 2016b, Astron. Nachr., 337, 356
Chartas, G., Krawczynski, H., Zalesky, L., et al. 2017, ApJ, 837, 26

Chen, B., Dai, X., Kochanek, C. S., et al. 2011, ApJ, 740, L34
Chen, B., Dai, X., Kochanek, C. S., et al. 2012, ApJ, 755, 24
Crenshaw, D. M., & Kraemer, S. B. 2012, ApJ, 753, 75
Dadina, M., Vignali, C., Cappi, M., et al. 2018, A&A, 610, L13
Dai, X., Chartas, G., Agol, E., Bautz, M. W., & Garmire, G. P. 2003, ApJ, 589, 100
Di Matteo, T., Springel, V., & Hernquist, L. 2005, Nature, 433, 604
Duras, F., Bongiorno, A., Ricci, F., et al. 2020, A&A, 636, A73
Fedorova, E. V., Zhdanov, V. I., Vignali, C., & Palumbo, G. G. C. 2008, A&A, 490, 989
Fiore, F., Feruglio, C., Shankar, F., et al. 2017, A&A, 601, A143
Giustini, M., Cappi, M., Chartas, G., et al. 2011, A&A, 536, A49
Gofford, J., Reeves, J. N., Tombesi, F., et al. 2013, MNRAS, 430, 60
Gofford, J., Reeves, J. N., Braito, V., et al. 2014, ApJ, 784, 77
Guerras, E., Dai, X., Steele, S., et al. 2017, ApJ, 836, 206
Hasinger, G., Schartel, N., & Komossa, S. 2002, ApJ, 573, L77
Hopkins, P. F., & Elvis, M. 2010, MNRAS, 401, 7
Huchra, J., Gorenstein, M., Kent, S., et al. 1985, AJ, 90, 691
Igo, Z., Parker, M. L., Matzeu, G. A., et al. 2020, MNRAS, 493, 1088
Jaffe, W., Meisenheimer, K., Röttgering, H. J. A., et al. 2004, Nature, 429, 47
Just, D. W., Brandt, W. N., Shemmer, O., et al. 2007, ApJ, 665, 1004
Kalberla, P. M. W., Burton, W. B., Hartmann, D., et al. 2005, A&A, 440, 775
Kallman, T., & Bautista, M. 2001, ApJS, 133, 221
King, A., & Pounds, K. 2015, ARA&A, 53, 115
Kormendy, J., & Ho, L. C. 2013, ARA&A, 51, 511
Krawczynski, H., & Chartas, G. 2017, ApJ, 843, 118
Krawczynski, H., Chartas, G., & Kislat, F. 2019, ApJ, 870, 125
Lanzuisi, G., Giustini, M., Cappi, M., et al. 2012, A&A, 544, A2
Leahy, D. A. 2001, ApJ, 547, 449
Lusso, E., Comastri, A., Simmons, B. D., et al. 2012, MNRAS, 425, 623
Makishima, K. 1986, in Iron Lines from Galactic and Extragalactic X-ray Sources, eds. K. O. Mason, M. G. Watson, & N. E. White, 249
McConnell, N. J., Ma, C.-P., Gebhardt, K., et al. 2011, Nature, 480, 215
Mizumoto, M., Izumi, T., & Kohno, K. 2019, ApJ, 871, 156
Mosquera, A. M., & Kochanek, C. S. 2011, ApJ, 738, 96
Mosquera, A. M., Kochanek, C. S., Chen, B., et al. 2013, ApJ, 769, 53
Perola, G. C., Matt, G., Cappi, M., et al. 2002, A&A, 389, 802
Piconcelli, E., Jimenez-Bailón, E., Guainazzi, M., et al. 2005, A&A, 432, 15
Planck Collaboration VI. 2020, A&A, in press, https://doi.org/10.1051/0004-6361/201833910
Ponti, G., Papadakis, I., Bianchi, S., et al. 2012, A&A, 542, A83
Popović, L. Č., Jovanović, P., Mediavilla, E., et al. 2006, ApJ, 637, 620
Protassov, R., van Dyk, D. A., Connors, A., Kashyap, V. L., & Siemiginowska, A. 2002, ApJ, 571, 545
Reynolds, M. T., Walton, D. J., Miller, J. M., & Reis, R. C. 2014, ApJ, 792, L19
Richards, G. T., Lacy, M., Storrie-Lombardi, L. J., et al. 2006, ApJS, 166, 470
Risaliti, G., Salvati, M., Elvis, M., et al. 2009, MNRAS, 393, L1
Schmidt, R., Webster, R. L., & Lewis, G. F. 1998, MNRAS, 295, 488
Schneider, D. P., Turner, E. L., Gunn, J. E., et al. 1988, AJ, 95, 1619
Smith, R. N., Tombesi, F., Veilleux, S., Lohfink, A. M., & Luminari, A. 2019, ApJ, 887, 69
Tombesi, F., Cappi, M., Reeves, J. N., et al. 2010, A&A, 521, A57
Tombesi, F., Cappi, M., Reeves, J. N., et al. 2011, ApJ, 742, 44
Tombesi, F., Cappi, M., Reeves, J. N., & Braito, V. 2012, MNRAS, 422, L1
Tombesi, F., Cappi, M., Reeves, J. N., et al. 2013, MNRAS, 430, 1102
Vignali, C., Brandt, W. N., Schneider, D. P., & Kaspi, S. 2005, AJ, 129, 2519
Vignali, C., Iwasawa, K., Comastri, A., et al. 2015, A&A, 583, A141
Walton, D. J., Nardini, E., Gallo, L. C., et al. 2019, MNRAS, 484, 2544
Wambsganss, J., Brunner, H., Schindler, S., & Falco, E. 1999, A&A, 346, L5
Wertz, O., & Surdej, J. 2014, MNRAS, 442, 428
Yee, H. K. C. 1988, AJ, 95, 1331

Appendix A: *Chandra* stacked spectra

After analyzing the spectral properties of each *Chandra* observation, we inspected the stacked spectra to see the persistence of the features we found in the *Chandra* data and how these compare to those in the *XMM-Newton* data. First, we produced the individual-image stacked spectra combining all the epochs (Appendix A.1), then we combined all the images from all the epochs to obtain the final stacked spectrum (Appendix A.2). All the spectra were combined through the CIAO tool `combine_spectra`, then grouped to obtain at least 20 cts/bin, and analyzed applying the χ^2 statistics. All the best-fit values for each tested model are summarized in Table A.1.

A.1. Stacked spectra of the individual images

The single-image stacked spectra (total source time of 749 ks per image) of images B, C, and D show a similar number of counts in the 0.4–7 keV observed-energy band (5500 cts, 3975 cts, and 4766 cts, respectively), comparable to that of XMM 2002 and 2018, while for image A we obtain much better statistics (17 700 cts). The analysis applied to these spectra follows the same logic used for the *XMM-Newton* data. In Fig. A.1 we show the best-fit residuals to Model pl of the four stacked spectra. The best-fit values of the photon index are consistent across the four images (see Table A.1). All images show hints of absorption in the soft-energy band but these appear to be more prominent in image A. Moreover, they all present signatures of strong emission lines between 5 and 7 keV. Interestingly, images A, B, and D show hints of a line around 6.4 keV, while for image C it seems to be placed at slightly lower energies (≃5.5 keV). Hints of an absorption line at ≃7.4 keV seem to be present in images A and D but not in images B and C. Regarding the hard-energy end of the spectra, none show hints of reflection since residuals above 8 keV rest frame appear to be quite flat (although noisy).

We searched for an additional absorption component in each stacked spectrum through the same models used in Sect. 4 (Model pl_a and Model pl_pca). All four images require extra absorption and are best reproduced by a partial covering medium placed at the quasar's redshift (best-fit values in Table A.1). By superposing the $\Gamma - N_{\rm H}$ contours, we find that the column density is consistent within 1σ errors for all the stacked images. In terms of photon index, $\Gamma_{\rm B}$, $\Gamma_{\rm C}$, and $\Gamma_{\rm D}$ are consistent within 1σ, while $\Gamma_{\rm A}$, being the steepest, is consistent with the others only within 2.6σ. Regarding the superposed $N_{\rm H} - {\rm CF}$ contours, the best-fit values to both the parameters are consistent within 1.6σ for all the four images. The best-fit residuals of each spectrum to Model pl_pca still show hints of the lines discussed above.

Images A, B, and D show a highly significant Fe Kα emission line between ≃6.4 and 6.6 keV, which we first constrained as a narrow Gaussian component (Model pl_pca_el, Table A.1). Regarding image C, we find a highly significant narrow line placed at lower energies (≃5.6 keV), while we only marginally detect the Fe Kα at 6.4 keV (see Table A.1). Given the results obtained by Reynolds et al. (2014) over the combined spectra of all images from all epochs, we searched for broad emission lines in the single-image stacked spectra. When letting the width of these lines vary, the improvement in the goodness of the fit is highly significant only for image D ($\Delta\chi^2 = 11.0$ for $\Delta\nu = 1$), with new best-fit parameters $E_{\rm rf} = 6.28 \pm 0.20$ keV and $\sigma = 0.41^{+0.14}_{-0.18}$ keV. We marginally detect a broad emission line in image A ($E = 6.45 \pm 0.08$ keV, $\sigma = 0.16 \pm 0.09$ keV) and image B ($E_{\rm rf} = 6.18^{+0.43}_{-0.30}$ keV, $\sigma = 0.47^{+0.23}_{-0.35}$ keV), while for image C the data are best reproduced by a narrow line. The resolved width found for the emission lines can be explained as follows. From the HSS (see Sect. 3.2), we know that the Fe Kα is probably microlensed, thus its energy likely varies from epoch to epoch at a fixed image. Detecting a broad Fe Kα line in the single-image stacked spectra can be interpreted as indicating that the microlensing of the line at energies near the intrinsic energy of 6.4 keV is the most frequent effect, while those events producing more extreme energy shifts are more rare or less effective, as also shown in Chartas et al. (2016b) for RX J1131–1231.

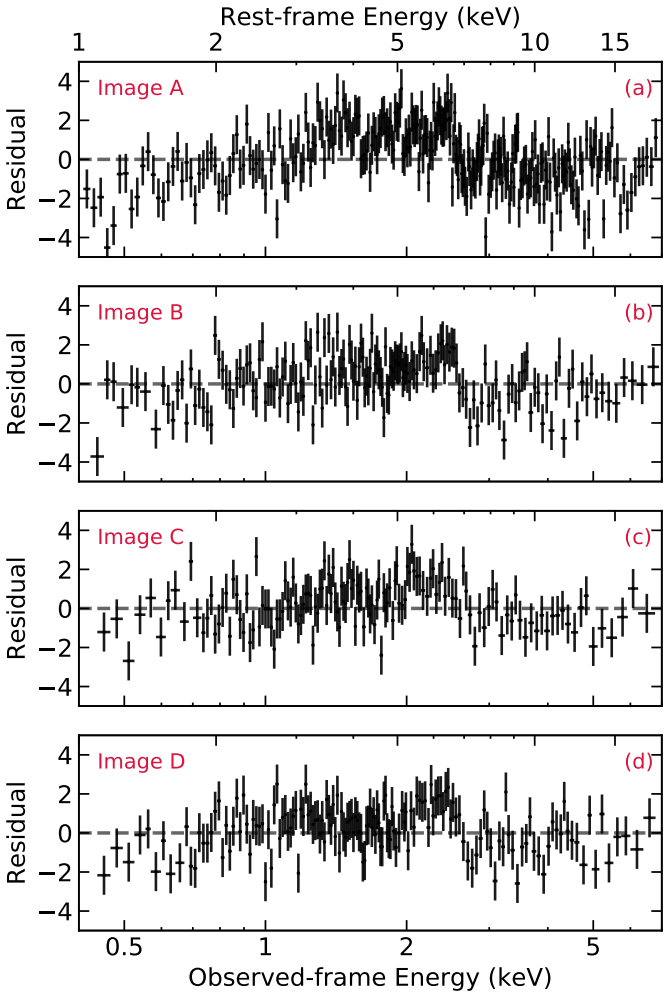

Fig. A.1. Rest-frame best-fit residuals of the individual-image stacked spectra to Model pl. *From top to bottom*: residuals of image A, B, C, and D.

The narrow absorption line is marginally detected (at 90%–99% confidence) at $E_{\rm rf} \simeq 7.3$–7.5 keV in the stacked spectra of images A, B, and D (best-fit parameters in Table A.1). However, as the residuals in Fig. A.1 suggest, it is not required for image C.

To summarize, we find that the cold and partial covering absorber and intrinsic emission are common to all the individual-image stacked spectra, although image A shows a slightly steeper photon index. This supports our previous result in which the absorber's column density was dominated by the in situ component (see Sect. 3). Regarding the narrow features, however, it is harder to provide a uniform description of the four spectra. On the one hand, image C is surely the most peculiar since it is the only one that presents an emission line at ≃5.6 keV (consistent with being narrow) and a marginally detected Fe Kα. In addition, it does not even show hints of the absorption line at

Table A.1. Summary of the best-fit parameters of each model tested for the *Chandra* stacked spectra.

Model	Image	Γ	$N_{\rm H}$	CF	$E_{\rm el}$	$\sigma_{\rm el}$	$E_{\rm al}$	$\sigma_{\rm al}$	$\chi^2_{\rm r}$ (ν)
pl	A	1.67 ± 0.03	–	–	–	–	–	–	2.20 (260)
pl	B	1.64 ± 0.03	–	–	–	–	–	–	1.58 (166)
pl	C	1.64 ± 0.03	–	–	–	–	–	–	1.40 (138)
pl	D	1.62 ± 0.03	–	–	–	–	–	–	1.39 (153)
pl_pca	A	2.07 ± 0.06	$4.53^{+0.88}_{-0.85}$	0.59 ± 0.04	–	–	–	–	1.42 (258)
pl_pca	B	1.96 ± 0.10	$3.44^{+1.68}_{-1.49}$	0.55 ± 0.08	–	–	–	–	1.29 (164)
pl_pca	C	1.98 ± 0.14	$5.85^{+2.87}_{-2.73}$	0.51 ± 0.11	–	–	–	–	1.22 (136)
pl_pca	D	1.89 ± 0.10	$2.73^{+1.70}_{-1.48}$	0.53 ± 0.12	–	–	–	–	1.16 (151)
pl_pca_el	A	2.05 ± 0.06	$4.09^{+0.86}_{-0.82}$	0.58 ± 0.04	6.49 ± 0.08	<0.01	–	–	1.28 (256)
pl_pca_el	B	1.95 ± 0.10	$3.04^{+1.58}_{-1.42}$	0.55 ± 0.08	$6.60^{+0.13}_{-0.22}$	<0.01	–	–	1.20 (162)
pl_pca_el (1)	C	1.91 ± 0.14	$4.45^{+3.11}_{-2.97}$	$0.46^{+0.11}_{-0.14}$	5.56 ± 0.08	<0.01	–	–	1.12 (134)
pl_pca_el (2)	C	1.95 ± 0.14	$5.08^{+2.90}_{-2.77}$	$0.49^{+0.10}_{-0.13}$	$6.37^{+0.20}_{-0.34}$	<0.01	–	–	1.19 (134)
pl_pca_el	D	1.89 ± 0.10	$2.40^{+1.59}_{-1.41}$	$0.53^{+0.18}_{-0.11}$	$6.50^{+0.13}_{-0.23}$	<0.01	–	–	1.07 (149)
pl_pca_bel	A	2.05 ± 0.06	3.93 ± 0.84	0.58 ± 0.04	6.45 ± 0.08	0.16 ± 0.08	–	–	1.27 (255)
pl_pca_bel	B	1.92 ± 0.10	$2.32^{+1.58}_{-1.45}$	$0.54^{+0.19}_{-0.11}$	$6.18^{+0.43}_{-0.30}$	$0.47^{+0.23}_{-0.35}$	–	–	1.17 (161)
pl_pca_bel	C	1.85 ± 0.13	$2.52^{+3.28}_{-2.20}$	$0.42_{-0.16}$	5.94 ± 0.23	$0.52^{0.24}_{-0.17}$	–	–	1.09 (133)
pl_pca_bel	D	1.88 ± 0.10	$1.90^{+1.50}_{-1.38}$	$0.54_{-0.13}$	6.28 ± 0.20	$0.41^{+0.14}_{-0.18}$	–	–	1.00 (148)
pl_pca_el_al	A	2.05 ± 0.06	4.18 ± 0.85	0.58 ± 0.04	6.49 ± 0.08	<0.01	$7.26^{+0.19}_{-0.15}$	<0.01	1.27 (254)
pl_pca_el_al	B	1.94 ± 0.10	$3.11^{+1.63}_{-1.46}$	0.54 ± 0.09	$6.60^{+0.14}_{-0.22}$	<0.01	$7.49^{+0.19}_{-0.21}$	<0.01	1.17 (160)
pl_pca_el_al	C	1.91 ± 0.14	$4.60^{3.20}_{-2.99}$	$0.45^{+0.11}_{-0.14}$	5.57 ± 0.08	<0.01	$7.57^{+0.40}_{-0.22}$	<0.01	1.12 (132)
pl_pca_el_al	D	1.87 ± 0.10	$2.43^{+1.63}_{-1.44}$	$0.53^{+0.17}_{-0.11}$	$6.50^{+0.13}_{-0.23}$	<0.01	7.41 ± 0.17	<0.01	1.04 (147)
pl_pca_el	A+B+D	1.99 ± 0.05	3.65 ± 0.69	0.54 ± 0.04	6.50 ± 0.06	>0.01	–	–	1.27 (305)
pl_pca_bel	A+B+D	1.98 ± 0.05	3.36 ± 0.70	0.54 ± 0.04	$6.43^{+0.07}_{-0.26}$	$0.23^{+0.23}_{-0.08}$	–	–	1.21 (304)
pl	A+B+C+D	1.66 ± 0.02	–	–	–	–	–	–	2.48 (319)
pl_pca	A+B+C+D	2.00 ± 0.04	$4.43^{+0.71}_{-0.69}$	0.55 ± 0.03	–	–	–	–	1.53 (317)
pl_pca_el	A+B+C+D	1.99 ± 0.04	3.48 ± 0.68	0.52 ± 0.04	6.49 ± 0.07	<0.01	–	–	1.32 (315)
pl_pca_el_al	A+B+C+D	1.98 ± 0.04	3.92 ± 0.69	0.53 ± 0.04	6.49 ± 0.07	<0.01	7.43 ± 0.09	<0.01	1.27 (313)
pl_pca_bel	A+B+C+D	1.95 ± 0.04	2.92 ± 0.70	0.51 ± 0.04	6.09 ± 0.14	0.52 ± 0.11	–	–	1.23 (314)
pl_pca_bel_al	A+B+C+D	1.94 ± 0.05	2.86 ± 0.73	0.50 ± 0.04	6.13 ± 0.14	$0.61^{+0.16}_{-0.13}$	7.36 ± 0.11	<0.01	1.17 (312)
pl_pca_bel_bal	A+B+C+D	1.93 ± 0.05	2.84 ± 0.75	0.50 ± 0.04	$6.30^{+0.24}_{-0.20}$	0.73 ± 0.16	7.28 ± 0.10	$0.26^{+0.16}_{-0.11}$	1.15 (311)
pl_pca_bel_el_al	A+B+C+D	1.96 ± 0.04	3.26 ± 0.68	0.52 ± 0.04	6.44 ± 0.07	0.22 ± 0.07	7.42 ± 0.10	<0.01	1.14 (310)
					5.62 ± 0.09	<0.01			

Notes. Column 1: model name; Col. 2: combined images; Col. 3: photon index; Col. 4: column density in excess of the Galactic value (units of 10^{22} cm^{-2}); Col. 5: covering fraction of the extra absorption; Col. 6: energy of the emission line (in units of keV); Col. 7: width of the emission line (in units of keV); Col. 8: energy of the absorption line (in units of keV); Col. 9: width of the absorption line (in units of keV); Col. 10: reduced χ^2 (degrees of freedom). All the errors are evaluated at 90% confidence. *Model list*: Model pl=phabs*zpo; Model pl_pca=phabs*zpcf*zpo; Model pl_pca_el=phabs*zpcf*(zpo+zgauss); Model pl_pca_el_al=phabs*zpcf*(zpo+zgauss+zgauss). When the width of the emission and absorption line is a free parameter of the model, it is reported as a bel/bal component in its name.

≃7.4 keV. On the other hand, the energies of the narrow Fe Kα from all the stacked images (also that of the marginal detection in image C) are consistent within 1σ, and so they remain if we consider the energy of the broad lines.

Moreover, since the stacking is of 37 epochs, we should bear in mind that these broad emission lines might not be intrinsically broad. They could likely be produced by the combination of single-epoch microlensed Fe Kα, which we actually see in the single-image spectra (Sect. 3.2). In this sense, the differences in significance we find between the four images are to be interpreted as the result of different microlensing events occurring in the respective image during the epochs. In conclusion, when stacking all the single-image spectra from all the epochs into one single spectrum, we should take into account all the properties found above, especially those we find in image C.

A.2. Stacked spectra of all images

The final stacked spectrum has a total exposure time of almost 3Ms and 32032 source net counts in the 0.4–7 keV observed-energy range. Its best-fit residuals to Model pl are shown in Fig. A.2, panel a. As expected from the results in the previous section, we find evidence of absorption in the soft-energy band, a prominent emission line at ≃6.5 keV that seems skewed at lower energies, and hints of an absorption line at ≃7.4 keV. Adding a partial covering cold absorber significantly improves the quality of the fit (see Table A.1). The best-fit parameters we obtain agree with those of the single images and the residuals still show an excess at ≃6.5 keV and a deficit of counts at ≃7.4 keV. By adding two narrow Gaussian components to the model, we find a highly significant emission line at $E_{\rm rf}$ = 6.49 ± 0.07 keV ($\Delta\chi^2/\Delta\nu = 70/2$) and an absorption line at $E_{\rm rf}$ = 7.43 ± 0.09 keV ($\Delta\chi^2/\Delta\nu = 18/2$). However, the residuals still indicate the emission line to be skewed at lower energies, so we let its width vary (Model pl_pca_bel_al). We find a much better best fit ($\Delta\chi^2 = 32.3$, $\Delta\nu = 1$), with a broad emission line at $E_{\rm rf} = 6.13 \pm 0.14$ keV and $\sigma = 0.61^{+0.16}_{-0.13}$ keV. When also allowing the absorption-line width to vary (Model pl_pca_bel_bal), we find it significantly ($\Delta\chi^2 = 10.1$, $\Delta\nu = 1$) consistent with being broad ($\sigma = 0.26^{+0.16}_{-0.11}$ keV) and placed at $E_{\rm rf} = 7.28 \pm 0.10$ keV. This also changes the centroid and the width of the emission line, which become $E_{\rm rf} = 6.29^{+0.24}_{-0.20}$ keV and $\sigma = 0.72 \pm 0.16$ keV.

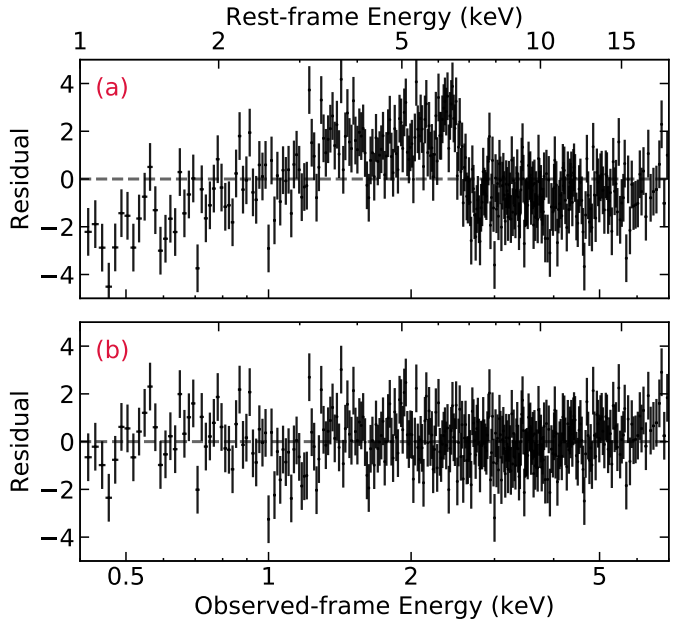

Fig. A.2. Best-fit residuals of the final *Chandra* spectrum to Model pl (*panel a*) and Model pl_pca_bel_el_al (*panel b*).

However, the best-fit residuals of Model pl_pca_bel_bal indicate that the model is overestimating (underestimating) the data at energies lower (higher) than the best-fit centroid of the emission line. This could be the indication of a relativistically blurred Fe Kα line. In fact, the energy and width we find using Model pl_pca_bel_al are consistent with those found by Reynolds et al. (2014), which they interpret as the indication of a relativistically broadened line. If we exclude the absorption line from the model, we find the same skewed centroid energy and width as in the preliminary analysis done by Reynolds et al. (2014).

However, based on the single-image stacked-spectra results, the width of the emission line could be artificially produced by the stacking, since the line in image C is placed at lower energies with regard to the other three (see Fig. A.1). Thus, we produced a new stacked spectrum, combining all the epochs of only images A, B, and D. Considering the absorber and the emission feature (Model pl_pca_bel), we find that the line is less broad ($\sigma = 0.23^{+0.23}_{-0.08}$ keV) and, more importantly, its centroid is placed at higher energies ($E_{\rm rf} = 6.43^{+0.07}_{-0.26}$ keV). Moreover, constraining the width of the line to be lower than the CCD resolution or letting it vary freely make almost no difference on a statistical basis (see Table A.1). Finally, if we compute the F-test significance for the addition of the width as a free parameter, we find that it is not required by the data. Thus, the skewed emission line we find at ≃6.13 keV is most probably generated by the blending of two distinct lines.

Given the results obtained with the combined spectrum of images A+B+D and those from the individual-image stacked spectra, we tried to model the skewed emission line as a narrow component plus a broad component, the first at ≃5.6 and the second at ≃6.5 keV (Model pl_pca_bel_el). This produced a $\Delta\chi^2 = 17.1$ for two parameters of interest (compared to Model pl_pca_bel), which according to the F-test translates into a detection above 99.99% confidence of the narrow line placed at $E_{\rm rf} = 5.62 \pm 0.08$ keV. The broad Fe Kα is now detected at $E_{\rm rf} = 6.44 \pm 0.07$ keV with $\sigma = 0.22 \pm 0.07$ keV, which is inconsistent with the centroid energy of the relativistically skewed line found by Reynolds et al. (2014) ($E_{\rm rf} = 6.58 \pm 0.03$ keV). We also detect the narrow absorption line at $E_{\rm rf} = 7.42 \pm 0.10$ keV (Model pl_pca_bel_el_al) at 99.8% confidence (from the F-test). This model also corresponds to the one that returns the best representation of the data, both on the basis of the distribution of the residuals (see Fig. A.2, panel b) and in terms of statistical improvement. This result corroborates our statement of the skewed line being the blending of the two lines we find in the individual-image staked spectra. Thus, when stacking the spectra of a gravitationally lensed quasar, checking the properties of each image is fundamental.

In conclusion, the spectral features of the stacked spectra confirm the presence of two distinct outflow components based on the following arguments. The absorption lines at higher energies (≃11.8 keV) of the single-epoch *Chandra* spectra are absent in the stacked spectra, whereas we detect (marginally or significantly) the absorption line at ≃7.4 keV. The 11.8 keV features are probably associated with an outflow whose ionization state (i.e., the absorption line energy) varies more rapidly than that of the wind producing the 7.4 keV line. Thus, it indicates that the two winds are consistent with being launched at different radii with regard to the central engine, meaning the one associated with the 11.8 keV is produced closer to the BH. Moreover, this scenario would also agree with that proposed in Sect. 5 based on the significance of the two lines in XMM 2002. This would imply the absence of lines in XMM 2018 as the indication that during the 2018 observation either both outflows are weak (in terms of velocity component along the line of sight) or that the outermost is weak and the other is so extremely ionized that it becomes undetectable.